

Comparing Probability Distributions with Conditional Transport

Huangjie Zheng and Mingyuan Zhou
The University of Texas at Austin

July 1, 2021

Abstract

To measure the difference between two probability distributions, we propose conditional transport (CT) as a new divergence and further approximate it with the amortized CT (ACT) cost to make it amenable to implicit distributions and stochastic gradient descent based optimization. ACT amortizes the computation of its conditional transport plans and comes with unbiased sample gradients that are straightforward to compute. When applied to train a generative model, ACT is shown to strike a good balance between mode covering and seeking behaviors and strongly resist mode collapse. On a wide variety of benchmark datasets for generative modeling, substituting the default statistical distance of an existing generative adversarial network with ACT is shown to consistently improve the performance.

1 Introduction

Measuring the difference between two probability distributions is a fundamental problem in statistics and machine learning [Cover, 1999, Bishop, 2006, Murphy, 2012]. A variety of statistical distances have been proposed to quantify the difference, which often serves as the first step to build a generative model. Commonly used statistical distances include the Kullback–Leibler (KL) divergence [Kullback and Leibler, 1951], Jensen–Shannon (JS) divergence [Lin, 1991], and Wasserstein distance [Kantorovich, 2006]. While being widely used for generative modeling [Kingma and Welling, 2013, Goodfellow et al., 2014, Arjovsky et al., 2017, Balaji et al., 2019], they all have their own limitations. The KL divergence, directly related to both maximum likelihood estimation and variational inference, is amenable to mini-batch stochastic gradient descent (SGD) based optimization [Wainwright and Jordan, 2008, Hoffman et al., 2013, Blei et al., 2017]. However, it requires the two probability distributions to share the same support, and hence is often inapplicable if either is an implicit distribution whose probability density function (PDF) is unknown [Mohamed and Lakshminarayanan, 2016, Huszár, 2017, Tran et al., 2017, Yin and Zhou, 2018]. The JS divergence is directly related to the mini-max loss of a generative adversarial net (GAN) when the discriminator is optimal [Goodfellow et al., 2014]. However, it is difficult to maintain a good balance between the generator and discriminator, making GANs notoriously brittle to train. The Wasserstein distance is a widely used metric that allows the two distributions to have non-overlapping supports [Villani, 2008, Santambrogio, 2015, Peyré and Cuturi, 2019]. To utilize it to build a generative model, one often employs its dual form that comes with a critic, which generally results in biased sample gradients [Arjovsky et al., 2017, Bellemare et al., 2017]. One may also consider the primal form and approximate it with the expected sample Wasserstein distance, which provides an asymptotic approximation of the Wasserstein distance but suffers from high computational cost [Bottou et al., 2017, Bińkowski et al., 2018, Bernton et al., 2019].

To address the limitations of existing measurement methods, we introduce conditional transport (CT) as a new divergence to quantify the difference between two probability distributions. We refer to them as the source and target distributions and denote their probability density functions (PDFs) as $p_X(\mathbf{x})$ and $p_Y(\mathbf{y})$, respectively. The CT divergence is defined with a bidirectional distribution-to-distribution transport. It consists of a forward CT that transports the source to target distribution, and a backward CT that reverses the transport direction. Our intuition is that given a source (target) point, it is more likely to be transported to a target (source) point closer to it. More specifically, if the target distribution

does not provide a good coverage of the source density, then there will exist source data points that lie in low density regions of the target (source), making the transport cost of the forward CT be high. Therefore, we expect that minimizing the forward CT will encourage the target distribution to exhibit a mode covering behavior with respect to (w.r.t.) the source PDF. Similarly, we expect that minimizing the backward CT will encourage the target distribution to exhibit a mode seeking behavior w.r.t. the source PDF.

Denoting $d(\mathbf{x}, \mathbf{y}) = d(\mathbf{y}, \mathbf{x})$ as a learnable function and $c(\mathbf{x}, \mathbf{y}) = c(\mathbf{y}, \mathbf{x}) \geq 0$, where the equality is true when $\mathbf{x} = \mathbf{y}$, as the point-to-point transport cost, the goal is to minimize the transport cost between two distributions. The forward CT is constructed in three steps: 1) We define a forward “navigator” as $\pi(\mathbf{y} | \mathbf{x}) = e^{-d(\mathbf{x}, \mathbf{y})} p_Y(\mathbf{y}) / \int e^{-d(\mathbf{x}, \mathbf{y})} p_Y(\mathbf{y}) d\mathbf{y}$, a conditional distribution specifying how likely a given source point \mathbf{x} will be transported to distribution $p_Y(\mathbf{y})$ via path $\mathbf{x} \rightarrow \mathbf{y}$; 2) We define the cost of a forward \mathbf{x} -transporting CT as $\int c(\mathbf{x}, \mathbf{y}) \pi(\mathbf{y} | \mathbf{x}) d\mathbf{y}$, the expected cost of employing the forward navigator to transport \mathbf{x} to a random target point; 3) We define the total cost of the forward CT as $\int p_X(\mathbf{x}) \int c(\mathbf{x}, \mathbf{y}) \pi(\mathbf{y} | \mathbf{x}) d\mathbf{y} d\mathbf{x}$, which is the expectation of the cost of a forward \mathbf{x} -transporting CT with respect to $p_X(\mathbf{x})$. Similarly, we construct the backward CT by first defining a backward navigator as $\pi(\mathbf{x} | \mathbf{y}) = e^{-d(\mathbf{x}, \mathbf{y})} p_X(\mathbf{x}) / \int e^{-d(\mathbf{x}, \mathbf{y})} p_X(\mathbf{x}) d\mathbf{x}$. Estimating CT involves both $\pi(\mathbf{x} | \mathbf{y})$ and $\pi(\mathbf{y} | \mathbf{x})$, which, however, are generally intractable to evaluate and sample from, unless both $p_X(\mathbf{x})$ and $p_Y(\mathbf{y})$ are conjugate priors for likelihood $e^{-d(\mathbf{x}, \mathbf{y})}$, i.e., $\pi(\mathbf{x} | \mathbf{y})$ and $\pi(\mathbf{y} | \mathbf{x})$ are in the same probability distribution family as $p_X(\mathbf{x})$ and $p_Y(\mathbf{y})$, respectively.

To apply the CT divergence in a general setting where we only have access to random samples from the distributions, we approximate it with the amortized CT (ACT) cost, which is amenable to mini-batch SGD based optimization. Similar to how the expected sample Wasserstein distance is defined to approximate the Wasserstein distance [Bernton et al., 2019], we define the ACT cost as the expected sample CT cost, which is the expected value of the CT cost, whose $p_X(\mathbf{x})$ and $p_Y(\mathbf{y})$ are both replaced with their discrete empirical distributions, respectively supported on N independent, and identically distributed (*iid*) random samples from $p_X(\mathbf{x})$ and M *iid* random samples from $p_Y(\mathbf{y})$. ACT is asymptotically equivalent to CT when both $N \rightarrow \infty$ and $M \rightarrow \infty$. Intuitively, it can also be interpreted as performing both a forward one-to- M stochastic CT from the source to target and a backward one-to- N stochastic CT from the target to source, with the expected cost providing an unbiased sample estimate of the ACT cost.

We show that similar to the KL divergence, ACT provides unbiased sample gradients, but different from it, neither $p_X(\mathbf{x})$ nor $p_Y(\mathbf{y})$ needs to be known. Similar to the Wasserstein distance, it does not require the distributions to share the same support. Different from the Wasserstein distance in its dual form, the sample estimates of ACT and its gradients are unbiased. Different from the expected sample Wasserstein distance and its entropy smoothed variations, the sample estimates of ACT are straightforward to compute as no inner loops are required. In GANs or Wasserstein GANs [Arjovsky et al., 2017], having an optimal discriminator or critic is required to unbiasedly estimate the JS divergence or Wasserstein distance and hence the gradients of the generator [Bottou et al., 2017]. However, this is rarely the case in practice, motivating a common remedy to stabilize the training by carefully regularizing the gradients, such as clipping or normalizing their values [Gulrajani et al., 2017, Miyato et al., 2018]. By contrast, in an adversarial game under ACT, regardless of how well the critic, which manipulates the point-to-point transport cost $c(\mathbf{x}, \mathbf{y})$ and the navigators’ conditional distributions for $\mathbf{x} \rightarrow \mathbf{y}$ and $\mathbf{x} \leftarrow \mathbf{y}$, is optimized, the sample estimates of ACT stay unbiased.

To demonstrate the use of the ACT cost (or CT divergence), we apply it to train implicit (or explicit) distributions to model both 1D and 2D toy data, MNIST digits, and natural images. The implicit distribution is defined by a deep generative model (DGM) that is simple to sample from. We focus on adapting existing GANs, with minimal changes to their settings except for substituting the statistical distances in their loss functions with ACT. We leave tailoring the network architectures to ACT to future study. More specifically, we modify the GAN loss function to an adversarial game between a generator, a forward navigator, and a backward navigator, which try to minimize the distribution-to-distribution transport cost by optimizing both the fake data distribution $p_Y(\mathbf{y})$ and two conditional point-to-point navigation-path distributions $\pi(\mathbf{y} | \mathbf{x})$ and $\pi(\mathbf{x} | \mathbf{y})$, versus a critic that does the opposite by both inflating the point-to-point transport cost $c(\mathbf{x}, \mathbf{y})$ and distorting the feature space used to build the transport maps. Modifying an existing (Wasserstein) GAN with the ACT cost, our experiments show consistent improvements in not only quantitative performance and

generation quality, but also learning stability.

2 CT Generator, Navigators, and Critic

Denote \mathbf{x} as a data taking its value in \mathbb{R}^V . In practice, we observe a finite set $\mathcal{X} = \{\mathbf{x}_i\}_{i=1}^{|\mathcal{X}|}$, consisting of $|\mathcal{X}|$ data samples assumed to be *iid* drawn from $p_X(\mathbf{x})$. Given \mathcal{X} , the usual task is to learn a distribution to approximate $p_X(\mathbf{x})$, for which we consider a DGM defined as $\mathbf{y} = G_\theta(\epsilon)$, $\epsilon \sim p(\epsilon)$, where G_θ is a generator that transforms noise $\epsilon \sim p(\epsilon)$ via a deep neural network parameterized by θ to generate random sample $\mathbf{y} \in \mathbb{R}^V$. While the PDF of the generator, denoted as $p_\theta(\mathbf{y})$, is often intractable to evaluate, it is straightforward to draw $\mathbf{y} \sim p_\theta(\mathbf{y})$ with G_θ . Denote both $\mu(d\mathbf{x}) = p_X(\mathbf{x})d\mathbf{x}$ and $\nu(d\mathbf{y}) = p_\theta(\mathbf{y})d\mathbf{y}$ as continuous probability measures over \mathbb{R}^V , with $\mu(\mathbb{R}^V) = \int_{\mathbb{R}^V} p_X(\mathbf{x})d\mathbf{x} = 1$ and $\nu(\mathbb{R}^V) = \int_{\mathbb{R}^V} p_\theta(\mathbf{y})d\mathbf{y} = 1$. The Wasserstein distance in its primal form can be defined with Kantorovich’s optimal transport problem [Kantorovich, 2006, Villani, 2008, Santambrogio, 2015, Peyré and Cuturi, 2019]:

$$\begin{aligned}\mathcal{W}(\mu, \nu) &= \min_{\pi \in \Pi(\mu, \nu)} \left\{ \int_{\mathbb{R}^V \times \mathbb{R}^V} c(\mathbf{x}, \mathbf{y}) \pi(d\mathbf{x}, d\mathbf{y}) \right\} \\ &= \min_{\pi \in \Pi(\mu, \nu)} \left\{ \mathbb{E}_{(\mathbf{x}, \mathbf{y}) \sim \pi(\mathbf{x}, \mathbf{y})} [c(\mathbf{x}, \mathbf{y})] \right\},\end{aligned}\tag{1}$$

where the minimum is taken over $\Pi(\mu, \nu)$, defined as the set of all possible joint probability measures π on $\mathbb{R}^V \times \mathbb{R}^V$, with marginals $\pi(A, \mathbb{R}^V) = \mu(A)$ and $\pi(\mathbb{R}^V, A) = \nu(A)$ for any Borel set $A \subset \mathbb{R}^V$. When $c(\mathbf{x}, \mathbf{y}) = \|\mathbf{x} - \mathbf{y}\|$, we obtain the Wasserstein-1 distance, for which there exists a dual form according to the Kantorovich duality as $\mathcal{W}_1(\mu, \nu) = \sup_{f \in \text{Lip}^1} \{ \mathbb{E}_{\mathbf{x} \sim p_X(\mathbf{x})} [f(\mathbf{x})] - \mathbb{E}_{\mathbf{y} \sim p_Y(\mathbf{y})} [f(\mathbf{y})] \}$, where f is referred to as the “critic” and Lip^1 denotes the set of all 1-Lipschitz functions [Villani, 2008]. Intuitively, the critic f plays the role of “amortizing” the computation of the optimal transport plan. However, as it is difficult to ensure the 1-Lipschitz constraint, one often resorts to approximations [Arjovsky et al., 2017, Gulrajani et al., 2017, Wei et al., 2018, Miyato et al., 2018] that inevitably introduce bias into the estimation of \mathcal{W}_1 and its gradient [Bellemare et al., 2017, Bottou et al., 2017].

2.1 Forward and Backward Navigators and CT Plans

Constraining $\pi \in \Pi(\mu, \nu)$, the Wasserstein distance satisfies $\mathcal{W}(\mu, \nu) = \mathcal{W}(\nu, \mu)$. By contrast, the proposed divergence allows $\pi \notin \Pi(\mu, \nu)$. Denote $d_\phi(\mathbf{h}_1, \mathbf{h}_2) \in \mathbb{R}$ as a neural network based function parameterized by ϕ , which measures the difference between two vectors $\mathbf{h}_1, \mathbf{h}_2 \in \mathbb{R}^H$. We introduce a forward CT, whose transport cost is defined as

$$\begin{aligned}\mathcal{C}_{\phi, \theta}(\mu \rightarrow \nu) &= \mathbb{E}_{\mathbf{x} \sim p_X(\mathbf{x})} \mathbb{E}_{\mathbf{y} \sim \pi_\phi(\mathbf{y} | \mathbf{x})} [c(\mathbf{x}, \mathbf{y})], \\ \pi_\phi(\mathbf{y} | \mathbf{x}) &\stackrel{\text{def.}}{=} \frac{e^{-d_\phi(\mathbf{x}, \mathbf{y})} p_\theta(\mathbf{y})}{\int e^{-d_\phi(\mathbf{x}, \mathbf{y})} p_\theta(\mathbf{y}) d\mathbf{y}},\end{aligned}\tag{2}$$

where $\pi_\phi(\mathbf{y} | \mathbf{x})$ will be analogized to the forward navigator that defines the forward CT plan. Similarly, we introduce the backward CT, whose transport cost is defined as

$$\begin{aligned}\mathcal{C}_{\phi, \theta}(\mu \leftarrow \nu) &= \mathbb{E}_{\mathbf{y} \sim p_\theta(\mathbf{y})} \mathbb{E}_{\mathbf{x} \sim \pi_\phi(\mathbf{x} | \mathbf{y})} [c(\mathbf{x}, \mathbf{y})], \\ \pi_\phi(\mathbf{x} | \mathbf{y}) &\stackrel{\text{def.}}{=} \frac{e^{-d_\phi(\mathbf{x}, \mathbf{y})} p_X(\mathbf{x})}{\int e^{-d_\phi(\mathbf{x}, \mathbf{y})} p_X(\mathbf{x}) d\mathbf{x}},\end{aligned}\tag{3}$$

where $\pi_\phi(\mathbf{x} | \mathbf{y})$ will be analogized to a backward navigator. We now define the CT problem as

$$\min_{\phi, \theta} \{ \mathcal{C}_{\phi, \theta}(\mu, \nu) \stackrel{\text{def.}}{=} \frac{1}{2} \mathcal{C}_{\phi, \theta}(\mu \rightarrow \nu) + \frac{1}{2} \mathcal{C}_{\phi, \theta}(\mu \leftarrow \nu) \},\tag{4}$$

where we refer to $\mathcal{C}_{\phi, \theta}(\mu, \nu)$ as the CT cost between μ and ν and $\text{argmin}_\phi \mathcal{C}_{\phi, \theta}(\mu, \nu)$ as the CT divergence. By definition we have $\text{argmin}_\phi \mathcal{C}_{\phi, \theta}(\mu, \nu) \geq 0$ and the two lemmas below further show that $\text{argmin}_\phi \mathcal{C}_{\phi, \theta}(\mu, \nu) = 0$ if and only if $\mu = \nu$.

Lemma 1. *If $\mathbf{y} \sim p_\theta(\mathbf{y})$ is equal to $\mathbf{x} \sim p_X(\mathbf{x})$ in distribution and d_ϕ is chosen such that $e^{-d_\phi(\mathbf{x}, \mathbf{y})} = \mathbf{1}(\mathbf{x} = \mathbf{y})$, where $\mathbf{1}(\cdot)$ equals to 1 if the condition is true and 0 otherwise, then both the joint probability measure π defined with $p_X(\mathbf{x})\pi_\phi(\mathbf{y} | \mathbf{x})$ in (2) and that with $p_\theta(\mathbf{y})\pi_\phi(\mathbf{x} | \mathbf{y})$ in (3) are in $\Pi(\mu, \nu)$.*

Lemma 2. If $\mathbf{y} \sim p_{\theta}(\mathbf{y})$ is equal to $\mathbf{x} \sim p_X(\mathbf{x})$ in distribution, then $\mathcal{C}_{\phi, \theta}(\mu, \nu) = \mathcal{C}_{\phi, \theta}(\mu \rightarrow \nu) = \mathcal{C}_{\phi, \theta}(\mu \leftarrow \nu) \geq \mathcal{W}(\mu, \nu) = 0$, where the equality can be achieved if $e^{-d_{\phi}(\mathbf{x}, \mathbf{y})} = \mathbf{1}(\mathbf{x} = \mathbf{y})$.

The proofs are deferred to Appendix A. Note in general, before both θ and ϕ reach their optimums, the conditions specified in Lemmas 1 and 2 are not satisfied and the joint probability measure π defined with $p_X(\mathbf{x})\pi_{\phi}(\mathbf{y}|\mathbf{x})$ or $p_{\theta}(\mathbf{y})\pi_{\phi}(\mathbf{x}|\mathbf{y})$ is not restricted to be in $\Pi(\mu, \nu)$, and hence it is possible for $\mathcal{C}_{\phi, \theta}(\mu \rightarrow \nu)$, $\mathcal{C}_{\phi, \theta}(\mu \leftarrow \nu)$, or $\mathcal{C}_{\phi, \theta}(\mu, \nu)$ to go below $\mathcal{W}(\mu, \nu)$ during training.

2.2 Amortized Conditional Transport

Computing the CT cost requires either knowing the PDFs of both navigators $\pi_{\phi}(\mathbf{y}|\mathbf{x})$ and $\pi_{\phi}(\mathbf{x}|\mathbf{y})$, or being able to draw random samples from them. However, usually neither is true unless both $p_{\theta}(\mathbf{y})$ and $p_X(\mathbf{x})$ are parametric prior distributions conjugate to $e^{-d_{\phi}(\mathbf{x}, \mathbf{y})}$. In the experimental results section, we will provide a univariate normal distribution based toy examples to illustrate this point. Below we show how to apply the CT cost in a general setting that only requires access to random samples of both \mathbf{x} and \mathbf{y} . While knowing neither $p_X(\mathbf{x})$ nor $p_{\theta}(\mathbf{y})$, we can obtain mini-batch based empirical probability measures $\hat{\mu}_N$ and $\hat{\nu}_M$, as defined below, to guide the optimization of G_{θ} in an iterative manner. With N random observations sampled without replacement from \mathcal{X} , we define

$$\hat{\mu}_N = \frac{1}{N} \sum_{i=1}^N \delta_{\mathbf{x}_i}, \quad \{\mathbf{x}_1, \dots, \mathbf{x}_N\} \subseteq \mathcal{X} \quad (5)$$

as an empirical probability measure for \mathbf{x} . Similarly, with M random samples of the generator, we define an empirical probability measure for \mathbf{y} as

$$\hat{\nu}_M = \frac{1}{M} \sum_{j=1}^M \delta_{\mathbf{y}_j}, \quad \mathbf{y}_j = G_{\theta}(\epsilon_j), \quad \epsilon_j \stackrel{iid}{\sim} p(\epsilon). \quad (6)$$

Substituting $p_{\theta}(\mathbf{y})$ in (2) with $\hat{\nu}_M(\mathbf{y})$, the continuous forward navigator becomes a discrete one as

$$\begin{aligned} \hat{\pi}_{\phi}(\mathbf{y}|\mathbf{x}) &= \sum_{j=1}^M \hat{\pi}_M(\mathbf{y}_j|\mathbf{x}, \phi) \delta_{\mathbf{y}_j}, \\ \hat{\pi}_M(\mathbf{y}_j|\mathbf{x}, \phi) &\stackrel{\text{def.}}{=} \frac{e^{-d_{\phi}(\mathbf{x}, \mathbf{y}_j)}}{\sum_{j'=1}^M e^{-d_{\phi}(\mathbf{x}, \mathbf{y}_{j'})}}. \end{aligned} \quad (7)$$

Thus the cost of a forward CT becomes

$$\begin{aligned} \mathcal{C}_{\phi, \theta}(\mu \rightarrow \hat{\nu}_M) &= \mathbb{E}_{\mathbf{x} \sim p_X(\mathbf{x})} [\mathcal{C}_{\phi, \theta}(\mathbf{x} \rightarrow \hat{\nu}_M)], \\ \mathcal{C}_{\phi, \theta}(\mathbf{x} \rightarrow \hat{\nu}_M) &\stackrel{\text{def.}}{=} \sum_{j=1}^M c(\mathbf{x}, \mathbf{y}_j) \hat{\pi}_M(\mathbf{y}_j|\mathbf{x}, \phi). \end{aligned} \quad (8)$$

In forward ACT, we expect large $c(\mathbf{x}, \mathbf{y}_j)$ to typically co-occur with small $\hat{\pi}_M(\mathbf{y}_j|\mathbf{x}, \phi)$ as long as $p_{\theta}(\mathbf{y})$ provides a good coverage of the density of \mathbf{x} . Thus minimizing the forward ACT cost is expected to encourage $p_{\theta}(\mathbf{y})$ to exhibit a mode covering behavior w.r.t. $p_X(\mathbf{x})$.

Similarly, we have the backward navigator and CT cost as

$$\begin{aligned} \hat{\pi}_{\phi}(\mathbf{x}|\mathbf{y}) &= \sum_{i=1}^N \hat{\pi}_N(\mathbf{x}_i|\mathbf{y}, \phi) \delta_{\mathbf{x}_i}, \\ \hat{\pi}_N(\mathbf{x}_i|\mathbf{y}, \phi) &\stackrel{\text{def.}}{=} \frac{e^{-d_{\phi}(\mathbf{x}_i, \mathbf{y})}}{\sum_{i'=1}^N e^{-d_{\phi}(\mathbf{x}_{i'}, \mathbf{y})}}, \\ \mathcal{C}_{\phi, \theta}(\hat{\mu}_N \leftarrow \nu) &= \mathbb{E}_{\mathbf{y} \sim p_{\theta}(\mathbf{y})} [\mathcal{C}_{\phi, \theta}(\hat{\mu}_N \leftarrow \mathbf{y})], \\ \mathcal{C}_{\phi, \theta}(\hat{\mu}_N \leftarrow \mathbf{y}) &\stackrel{\text{def.}}{=} \sum_{i=1}^N c(\mathbf{x}_i, \mathbf{y}) \hat{\pi}_N(\mathbf{x}_i|\mathbf{y}, \phi). \end{aligned} \quad (9)$$

In backward ACT, we expect large $c(\mathbf{x}_i, \mathbf{y})$ to typically co-occur with small $\hat{\pi}_N(\mathbf{x}_i|\mathbf{y}, \phi)$ as long as $p_X(\mathbf{x})$ has a good coverage of the density of \mathbf{y} . Thus minimizing the backward ACT cost is expected to encourage $p_{\theta}(\mathbf{y})$ to exhibit a mode seeking behavior w.r.t. $p_X(\mathbf{x})$.

Combining both the forward and backward CTs, we define the amortized CT (ACT) problem as

$$\min_{\phi, \theta} \{\mathcal{C}_{\phi, \theta}(\mu, \nu, N, M)\}, \quad (10)$$

where $\mathcal{C}_{\phi, \theta}(\mu, \nu, N, M)$ is the ACT cost defined as

$$\begin{aligned} \mathcal{C}_{\phi, \theta}(\mu, \nu, N, M) &= \frac{1}{2} \mathbb{E}_{\mathbf{y}_{1:M} \stackrel{iid}{\sim} p_{\theta}(\mathbf{y})} [\mathcal{C}_{\phi, \theta}(\mu \rightarrow \hat{\nu}_M)] \\ &\quad + \frac{1}{2} \mathbb{E}_{\mathbf{x}_{1:N} \stackrel{iid}{\sim} p_X(\mathbf{x})} [\mathcal{C}_{\phi, \theta}(\hat{\mu}_N \leftarrow \nu)]. \\ &= \frac{1}{2} \mathbb{E}_{\mathbf{y}_{1:M} \stackrel{iid}{\sim} p_{\theta}(\mathbf{y})} \mathbb{E}_{\mathbf{x} \sim p_X(\mathbf{x})} \left[\sum_{j=1}^M c(\mathbf{x}, \mathbf{y}_j) \frac{e^{-d_{\phi}(\mathbf{x}, \mathbf{y}_j)}}{\sum_{j'=1}^M e^{-d_{\phi}(\mathbf{x}, \mathbf{y}_{j'})}} \right] \\ &\quad + \frac{1}{2} \mathbb{E}_{\mathbf{x}_{1:N} \stackrel{iid}{\sim} p_X(\mathbf{x})} \mathbb{E}_{\mathbf{y} \sim p_{\theta}(\mathbf{y})} \left[\sum_{i=1}^N c(\mathbf{x}_i, \mathbf{y}) \frac{e^{-d_{\phi}(\mathbf{x}_i, \mathbf{y})}}{\sum_{i'=1}^N e^{-d_{\phi}(\mathbf{x}_{i'}, \mathbf{y})}} \right]. \end{aligned} \quad (11)$$

Lemma 3. *The ACT cost is asymptotic that $\lim_{N,M \rightarrow \infty} \mathcal{C}_{\phi,\theta}(\mu, \nu, N, M) = \mathcal{C}_{\phi,\theta}(\mu, \nu)$.*

Lemma 4. *Denoting $\hat{\mu}_N = \sum_{i=1}^N \frac{1}{N} \delta_{\mathbf{x}_i}$ and $\hat{\nu}_M = \sum_{j=1}^M \frac{1}{M} \delta_{\mathbf{y}_j}$, where $\mathbf{x}_{1:N} \stackrel{iid}{\sim} p_X(\mathbf{x})$ and $\mathbf{y}_{1:M} \stackrel{iid}{\sim} p_Y(\mathbf{y})$, and drawing $\mathbf{x} \sim \hat{\mu}_N$ and $\mathbf{y} \sim \hat{\nu}_M$, an unbiased sample estimator of the ACT cost can be expressed as*

$$\begin{aligned} \mathcal{L}_{\phi,\theta}(\mathbf{x}_{1:N}, \mathbf{y}_{1:M}) &= \frac{1}{2} \sum_{j=1}^M c(\mathbf{x}, \mathbf{y}_j) \hat{\pi}_M(\mathbf{y}_j | \mathbf{x}, \phi) \\ &\quad + \frac{1}{2} \sum_{i=1}^N c(\mathbf{x}_i, \mathbf{y}) \hat{\pi}_N(\mathbf{x}_i | \mathbf{y}, \phi). \end{aligned} \quad (12)$$

Intuitively, the first term in the summation can be interpreted as the expected cost of following the forward navigator to stochastically transport a random source point \mathbf{x} to one of the M randomly instantiated “anchors” of the target distribution. The second term shares a similar interpretation. Note in optimal transport, the Wasserstein distance $\mathcal{W}(\mu, \nu)$ in its primal form, shown in (1), is in general intractable to compute. To use the primal form, one often resorts to the sample Wasserstein distance defined as $\mathcal{W}(\hat{\mu}_N, \hat{\nu}_M)$, computing which, however, requires solving a combinatorial optimization problem [Peyré and Cuturi, 2019]. To make $\mathcal{W}(\hat{\mu}_N, \hat{\nu}_M)$ practical to compute, one remedy is to smooth the optimal transport plan between $\hat{\mu}_N$ and $\hat{\nu}_M$ with an entropic regularization term, resulting in the Sinkhorn distance that still requires to be estimated with an iterative procedure, whose convergence is sensitive to the entropic regularization coefficient [Cuturi, 2013, Genevay et al., 2016, 2018, Xie et al., 2020]. When the entropic regularization coefficient goes to infinity, we recover maximum mean discrepancy (MMD), which is considered as the metric for minimization, evaluated in a kernel space found by the adversarial mechanism in MMD-GAN [Li et al., 2015, 2017]. By contrast, equipped with two navigators, the ACT can directly compute a forward point-to-distribution transport cost, denoted as $\mathcal{C}_{\phi,\theta}(\mathbf{x} \rightarrow \hat{\nu}_M)$ in (8), and a backward one, denoted as $\mathcal{C}_{\phi,\theta}(\hat{\mu}_N \leftarrow \mathbf{y})$ in (9), which are then combined to define an unbiased sample estimator, as shown in (12), of the ACT cost. Intuitively, the navigators play the role of “amortizing” the computation of the CT plans between two empirical distributions, removing the need of using an iterative procedure to estimate the transport cost.

Lemma 5. *Another unbiased sample estimator fully using the data in mini-batches $\mathbf{x}_{1:N}$ and $\mathbf{y}_{1:M}$, computing an amortized transport cost between two empirical distributions, can be expressed as*

$$\begin{aligned} \mathcal{L}_{\phi,\theta}(\mathbf{x}_{1:N}, \mathbf{y}_{1:M}) &= \sum_{i=1}^N \sum_{j=1}^M c(\mathbf{x}_i, \mathbf{y}_j) \times \\ &\quad \left(\frac{1}{2N} \hat{\pi}_M(\mathbf{y}_j | \mathbf{x}_i, \phi) + \frac{1}{2M} \hat{\pi}_N(\mathbf{x}_i | \mathbf{y}_j, \phi) \right). \end{aligned} \quad (13)$$

2.3 Critic based Adversarial Feature Extraction

A naive definition of the transport cost between two points is some distance between their raw feature vectors, such as $c(\mathbf{x}, \mathbf{y}) = \|\mathbf{x} - \mathbf{y}\|_2^2$, which, however, often poorly reflects the difference between high-dimensional data residing on low-dimensional manifolds. For this reason, with cosine dissimilarity $\cos(\mathbf{h}_1, \mathbf{h}_2) \stackrel{\text{def}}{=} \frac{|\mathbf{h}_1^T \mathbf{h}_2|}{\sqrt{\mathbf{h}_1^T \mathbf{h}_1} \sqrt{\mathbf{h}_2^T \mathbf{h}_2}}$ [Salimans et al., 2018], we introduce a critic $\mathcal{T}_\eta(\cdot)$, parameterized by η , to help define an adversarial point-to-point transport cost as

$$c_\eta(\mathbf{x}, \mathbf{y}) = 1 - \cos(\mathcal{T}_\eta(\mathbf{x}), \mathcal{T}_\eta(\mathbf{y})). \quad (14)$$

Moreover, we incorporate this adversarial mechanism to redefine both navigators by substituting $d_\phi(\mathbf{x}, \mathbf{y})$ with

$$d_{\phi,\eta}(\mathbf{x}, \mathbf{y}) \stackrel{\text{def}}{=} d_\phi \left(\frac{\mathcal{T}_\eta(\mathbf{x})}{\|\mathcal{T}_\eta(\mathbf{x})\|}, \frac{\mathcal{T}_\eta(\mathbf{y})}{\|\mathcal{T}_\eta(\mathbf{y})\|} \right). \quad (15)$$

Intuitively, to optimize the generator by minimizing the distribution-to-distribution transport cost, both navigators try to optimize conditional path distributions, whereas the critic does the opposite by not only inflating the point-to-point transport cost, but also distorting the feature space used to construct the conditional transport maps.

In summary, given training data \mathcal{X} , to train the generator G_θ , forward navigator $\pi_\phi(\mathbf{y} | \mathbf{x})$, backward navigator $\pi_\phi(\mathbf{x} | \mathbf{y})$, and critic \mathcal{T}_η , we propose to solve a mini-max problem as

$$\min_{\phi, \theta} \max_{\eta} \mathbb{E}_{\mathbf{x}_{1:N} \subseteq \mathcal{X}, \mathbf{y}_{1:M} \stackrel{iid}{\sim} p(\mathbf{y})} [\mathcal{L}_{\phi,\theta,\eta}(\mathbf{x}_{1:N}, \{G_\theta(\mathbf{y}_j)\}_{j=1}^M)], \quad (16)$$

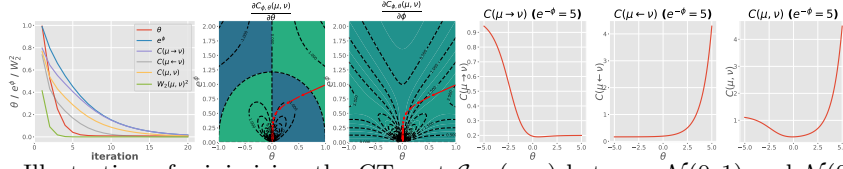


Figure 1: Illustration of minimizing the CT cost $\mathcal{C}_{\phi, \theta}(\mu, \nu)$ between $\mathcal{N}(0, 1)$ and $\mathcal{N}(0, e^\theta)$. *Left*: Evolution of CT cost, its parameters and forward and backward costs, and corresponding Wasserstein distance; *Middle*: Gradients of the CT w.r.t. θ or ϕ . The 2D trace of (θ, e^ϕ) is marked with red arrows. *Right*: The forward, backward, and CT values against θ when e^ϕ is optimized to a small value, which show combining forward and backward balances mode covering and seeking, making it easier for θ to move towards its optimum.

where $\mathcal{L}_{\phi, \theta, \eta}$ is defined the same as in (12) or (13), except that we replace $c(\mathbf{x}_i, \mathbf{y}_j)$ in them with $c_\eta(\mathbf{x}_i, \mathbf{y}_j)$ shown in (14), replace $d_\phi(\cdot, \cdot)$ in them with $d_{\phi, \eta}(\cdot, \cdot)$ shown in (15), and draw $\mathbf{y}_{1:M}$ using reparameterization as in (6), which means $\mathbf{y}_{1:M} \stackrel{\text{def.}}{=} \{G_\theta(\epsilon_j)\}_{j=1}^M$. With SGD, we train ϕ and θ using $\nabla_{\phi, \theta} \mathcal{L}_{\phi, \theta, \eta}(\mathbf{x}_{1:N}, \{G_\theta(\epsilon_j)\}_{j=1}^M)$ and, if the critic is employed, train η using $-\nabla_\eta \mathcal{L}_{\phi, \theta, \eta}(\mathbf{x}_{1:N}, \{G_\theta(\epsilon_j)\}_{j=1}^M)$.

Note in existing critic-based GANs, how well the critics are optimized are directly related to how accurate and stable the gradients can be estimated. By contrast, regardless of how well the critic is optimized to inflate $c_\eta(\mathbf{x}, \mathbf{y})$ and distort $d_{\phi, \eta}(\mathbf{x}, \mathbf{y})$, Lemma 4 shows the sample estimate $\mathcal{L}_{\phi, \theta, \eta}(\mathbf{x}_{1:N}, \{G_\theta(\epsilon_j)\}_{j=1}^M)$ of ACT and its gradients stay unbiased. Thus in ACT the critic can be pre-fixed, stopped at any time during the training, or trained using a different loss other than (16), such as the cross-entropy discriminator loss used in vanilla GANs to discriminate between \mathbf{x} and $G_\theta(\epsilon)$. This point will be verified in our ablation study.

3 Experimental Results

3.1 CT for Toy Data

As a proof of concept, we illustrate optimization under CT in 1D, with $x, y, \phi, \theta \in \mathbb{R}$. We consider a univariate normal distribution based example:

$$\begin{aligned} p(x) &= \mathcal{N}(0, 1), \quad p_\theta(y) = \mathcal{N}(0, e^\theta), \\ d_\phi(x, y) &= (x - y)^2 / (2e^\phi), \quad c(x, y) = (x - y)^2. \end{aligned} \quad (17)$$

Thus $\theta = 0$ is the optimal solution that makes $\nu = \mu$. Denote $\sigma(a) = 1/(1 + e^{-a})$ as the sigmoid function, we have analytic forms of the Wasserstein distance as $\mathcal{W}_2(\mu, \nu)^2 = (1 - e^{\frac{\theta}{2}})^2$, forward and backward navigators as $\pi_\phi(y|x) = \mathcal{N}(\sigma(\theta - \phi)x, \sigma(\theta - \phi)e^\phi)$ and $\pi_\phi(x|y) = \mathcal{N}(\sigma(-\phi)y, \sigma(\phi))$, and forward and backward CT costs as $\mathcal{C}_{\phi, \theta}(\mu \rightarrow \nu) = \sigma(\phi - \theta)(e^\theta + \sigma(\phi - \theta))$ and $\mathcal{C}_{\phi, \theta}(\mu \leftarrow \nu) = \sigma(\phi)(1 + \sigma(\phi)e^\theta)$ (see Appendix B.1 for more details). Thus when applying gradient descent to minimize the CT cost $\mathcal{C}_{\phi, \theta}(\mu, \nu)$, we expect the generator parameter $\theta \rightarrow 0$ as long as the learning rate of the navigator parameter ϕ is appropriately controlled to prevent $e^\phi \rightarrow 0$ from happening too soon. This is confirmed by Fig. 1, which shows that long before e^ϕ approaches zero, θ has already converged close to zero. This suggests that the navigator parameter ϕ mainly plays the role in assisting the learning of θ . It is also interesting to observe that the CT costs keep descending towards zero even when $\mathcal{W}_2(\mu, \nu)^2$ has already reached close to zero. As θ and ϕ converge towards their optimal solutions under the CT cost, we can observe that $\mathcal{C}_{\phi, \theta}(\mu \rightarrow \nu)$ and $\mathcal{C}_{\phi, \theta}(\mu \leftarrow \nu)$ are getting closer. Moreover, $\mathcal{C}_{\phi, \theta}(\mu, \nu)$ initially stays above $\mathcal{W}_2(\mu, \nu)^2 = (1 - e^{\frac{\theta}{2}})^2$ but eventually becomes very close to $\mathcal{W}_2(\mu, \nu)^2$, which agrees what Lemma 2 suggests.

The second and third subplots describe the descent trace on the gradient of the CT cost with respect to (w.r.t.) θ and ϕ , respectively, while the fourth to six subplots show the forward, backward, and bi-directional CT costs, respectively, against θ when e^ϕ is optimized close to its optimum (see Fig. 9 for analogous plots for additional values of e^ϕ). It is interesting to notice that the forward cost is minimized at $e^\theta > 1$, which implies mode covering, and the backward cost is minimized at $e^\theta \rightarrow 0$, which implies mode seeking, while the bi-directional cost is minimized at around the optimal solution $e^\theta = 1$; the forward CT cost exhibits a flattened curve on the right hand side of its minimum, adding to which the backward CT cost not only moves that minimum left, making it closer to $\theta = 0$, but also raises the whole curve on the right hand side, making the optimum of θ become easier to reach via gradient descent.

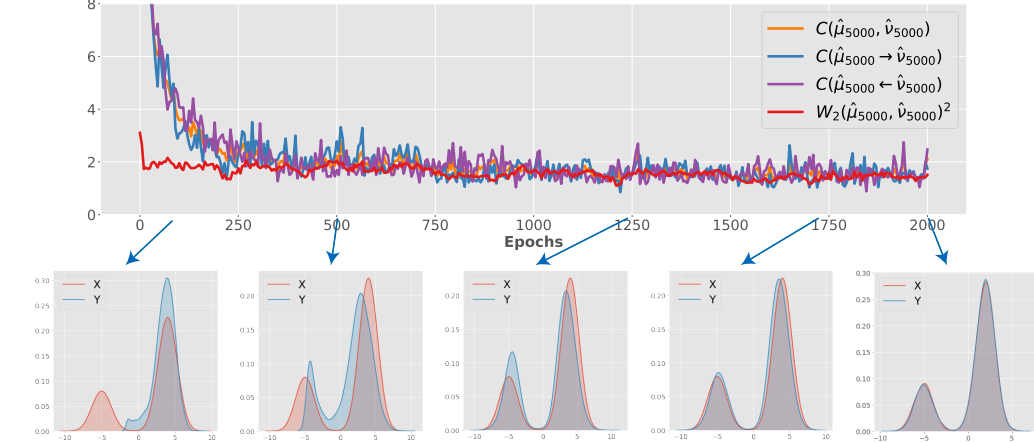


Figure 2: Illustration of how minimizing the ACT cost between the empirical distribution of a generator and that of a bimodal Gaussian mixture, whose 5000 random samples are given, helps optimize the generator distribution towards the true one. *Top*: Plots of the ACT cost $\mathcal{C}(\hat{\mu}_N, \hat{\nu}_M)$, forward ACT cost $\mathcal{C}(\hat{\mu}_N \rightarrow \hat{\nu}_M)$, backward ACT cost $\mathcal{C}(\hat{\mu}_N \leftarrow \hat{\nu}_M)$, and Wasserstein distance $\mathcal{W}_2(\hat{\mu}_N, \hat{\nu}_M)^2$, where $N = M = 5000$. *Bottom*: The PDF of the true data distribution $\mu(dx) = p_X(x)dx$ (red) and the generator distribution $\nu(dy) = p_\theta(y)dy$ (blue, visualized via kernel density estimation) at different training iterations.

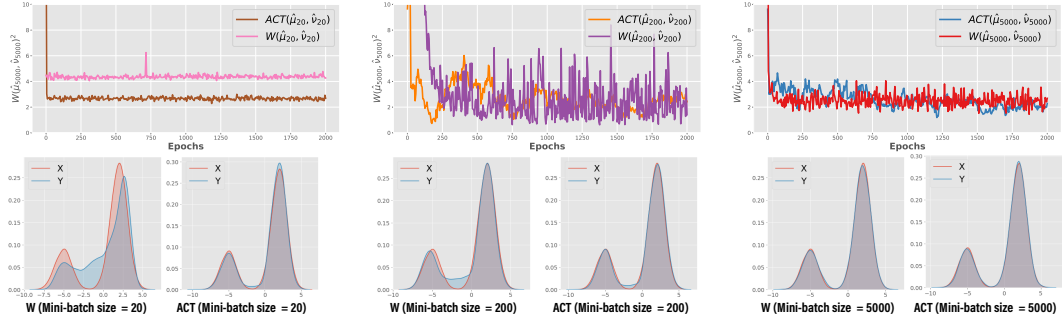


Figure 3: *Top*: Plot of the sample Wasserstein distance $\mathcal{W}_2(\hat{\mu}_{5000}, \hat{\nu}_{5000})^2$ against the number of training epochs, where the generator is trained with either $\mathcal{W}_2(\hat{\mu}_N, \hat{\nu}_N)^2$ or the ACT cost between $\hat{\mu}_N$ and $\hat{\nu}_N$, with the mini-batch size set as $N = 20$ (left), $N = 200$ (middle), or $N = 5000$ (right); one epoch consists of $5000/N$ SGD iterations. *Bottom*: The fitting results of different configurations, where the KDE curves of the data distribution and the generative one are marked in red and blue, respectively.

3.2 ACT for Generative Modeling

ACT for 1D toy data: We move on to model the empirical samples from a true data distribution, for which it is natural to apply ACT. We apply a deep neural network to generator G_θ and another one to \mathcal{T}_ϕ that is shared by both navigators. We consider the squared Euclidean (*i.e.* \mathcal{L}_2^2) distance to define both cost $c(\mathbf{x}, \mathbf{y})$ and distance $d(\mathbf{h}_1, \mathbf{h}_2)$. We first consider a 1D example, where \mathcal{X} consists of $|\mathcal{X}| = 5,000$ samples $x_i \in \mathbb{R}$ of a bimodal Gaussian mixture $p_X(x) = \frac{1}{4}\mathcal{N}(x; -5, 1) + \frac{3}{4}\mathcal{N}(x; 2, 1)$. We illustrate in Fig. 2 the training with unbiased sample gradients $\nabla_{\phi, \theta} \mathcal{L}_{\phi, \theta}(\mathcal{X}, y_{1:M})$ of the ACT cost shown in (13), where $y_j = G_\theta(\epsilon_j)$. The top panel shows the ACT cost, its backward and forward costs, and Wasserstein distance between the empirical probability measures $\hat{\mu}_N$ and $\hat{\nu}_M$ defined as in (5) and (6). We set $M = N$ and hence $\mathcal{W}_2(\hat{\mu}_X, \hat{\nu}_Y)^2$ can be exactly computed by sorting the 1D elements of $x_{1:N}$ and $y_{1:N}$ [Peyré and Cuturi, 2019]. We first consider $N = |\mathcal{X}| = 5000$. Fig. 2 (Top) shows that the ACT cost converges close to $\mathcal{W}_2(\hat{\mu}_X, \hat{\nu}_Y)^2$ and the forward and backward costs move closer to each other and can sometime go below $\mathcal{W}_2(\hat{\mu}_X, \hat{\nu}_Y)^2$. Fig. 2 (Bottom) shows that minimizing the ACT cost successfully drives the generator distribution towards true data density: From the left to right, we can observe that initially the generator is focused on fitting a single mode; at around the 500th iteration, as the forward and backward navigators are getting better, they start to help the generator locate the missing mode and we can observe a blue density mode starts to form over there; as the generator and both navigators are getting optimized, we can observe that the generator clearly captures both modes and the fitting is getting improved further; finally the generator well approximates the data density. Under the guidance of the ACT cost, the generator and navigators are

helping each other: An optimized generator helps the two navigators to train and realize the missing mode, and the optimized navigators help the generator locate under-fitted regions and hence better fit the true data density. Given the same \mathcal{X} , below we further consider setting $N = 20, 200$, or 5000 to train the generator, using either the Wasserstein distance $\mathcal{W}_2(\hat{\mu}_N, \hat{\nu}_N)^2$ or ACT cost $\mathcal{L}_{\phi, \theta}(x_{1:N}, y_{1:N})$ as the loss function.

As shown in Fig. 3 (right column), when the mini-batch size N is as large as 5000 , both Wasserstein and ACT lead to a well-trained generator. However, as shown in the left and middle columns, when N is getting much smaller, the generator trained with Wasserstein clearly underperforms that trained with ACT, especially when the mini-batch size becomes as small as $N = 20$. While the Wasserstein distance $\mathcal{W}(\mu, \nu)$ in theory can well guide the training of a generative model, the sample Wasserstein distance $\mathcal{W}(\hat{\mu}_N, \hat{\nu}_N)$, whose optimal transport plan is locally re-computed for each mini-batch, could be sensitive to the mini-batch size N , which also explains why in practice the sample Wasserstein-based generative models are difficult to train and desire a large mini-batch size [Salimans et al., 2018]. By contrast, ACT amortizes its conditional transport plans through its navigators, whose parameter ϕ is globally updated across mini-batches, leading to a well-trained generator whose performance has low sensitivity to the mini-batch size.

ACT for 2D toy data: We further conduct experiments on 4 representative 2D datasets: 8-Gaussian mixture, Swiss Roll, Half Moons, and 25-Gaussian mixture, whose results are shown in Figs. 10-13 of Appendix B.2. We apply the vanilla GAN [Goodfellow et al., 2014] and Wasserstein GAN with gradient penalty (WGAN-GP) [Gulrajani et al., 2017] as two representatives of mini-max DGMs that require solving a mini-max loss. We then apply the generators trained under the sliced Wasserstein distance (SWD) [Deshpande et al., 2018] and ACT cost as two representatives of mini-max-free DGMs. Compared to mini-max DGMs, which require an adversarially learned critic in order to train the generator, one clear advantage of mini-max-free DGMs is that the generator is stable to train without the need of an adversarial game. On each 2D data, we train these DGMs as one would normally do during the first $15k$ iterations. We then only train the generator and freeze all the other learnable model parameters, which means we freeze the discriminator in GAN, critic in WGAN, and the navigator parameter ϕ of the ACT cost, for another $15k$ iterations. Fig. 10 illustrates this training process on the 8-Gaussian mixture dataset, where for both mini-max DGMs, the mode collapse issue deteriorates after the first $15k$ iterations, while the training for SWD remains stable and that for ACT continues to improve. Compared to SWD, our method covers all 8 data density modes and moves the generator much closer to the true data density. On the other three datasets, the ACT based DGM also exhibits good training consistency, high stability, and close-to-optimal data generation performance, as shown in Appendix B.2.

Resistance to mode collapse: We use a 8-Gaussian mixture to empirically evaluate how well a DGM resists mode collapse. Unlike the data in Fig. 10, where 8 modes are equally weighted, here the mode at the left lower corner is set to have weight ρ while the other modes are set to have the same weight of $\frac{1-\rho}{7}$. We set \mathcal{X} with 5000 samples and the mini-batch size as $N = 100$. When ρ is lowered to 0.05 , its corresponding mode is shown to be missed by GAN, WGAN, and SWD-based DGM, while well kept by the ACT-based DGM. As an explanation, GANs are known to be susceptible to mode collapse; WGAN and SWD-based DGMs are sensitive to the mini-batch size, as when ρ equals to a small value, the samples from this mode will appear in the mini-batches less frequently than those from any other mode, amplifying their missing mode problem. Similarly, when ρ is increased to 0.5 , the other modes are likely to be missed by the baseline DGMs, while the ACT-based DGM does not miss any modes. The resistance of ACT to mode dropping can be attributed to the amortized computation of its conditional transport plans provided by the navigators, whose parameter is optimized with SGD over different mini-batches and, as indicated by Fig. 3, is robust to estimate across a wide range of mini-batch sizes.

Forward and backward analysis: To empirically verify our previous analysis of the mode covering (seeking) behavior of the forward (backward) ACT, we train a DGM by modifying (11) as ACT_γ , where $\gamma \in [0, 1]$ is the interpolation weight from the forward ACT cost to the backward one, which means ACT_γ reduces to the forward ACT when $\gamma = 1$, to backward ACT when $\gamma = 0$, and to the ACT in (11) when $\gamma = 0.5$. Fig. 5 shows the fitting results of ACT_γ on the same 1D bi-modal Gaussian mixture used in Fig. 2 and 2D 8-Gaussian mixture used in Fig. 10; the other experimental settings are kept the same. Comparing the results of different γ in Fig. 5 suggests that minimizing the forward transport cost only encourages the generator to exhibit mode covering behaviors, while minimizing the backward

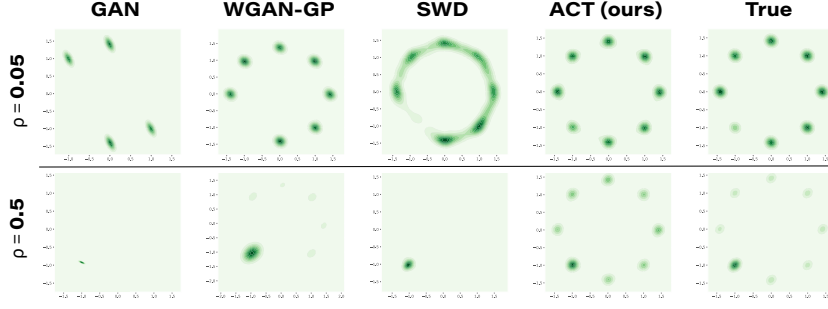


Figure 4: Comparison of the generation quality on 8-Gaussian mixture data: one of the 8 modes has weight ρ and the rest modes have equal weight as $\frac{1-\rho}{7}$.

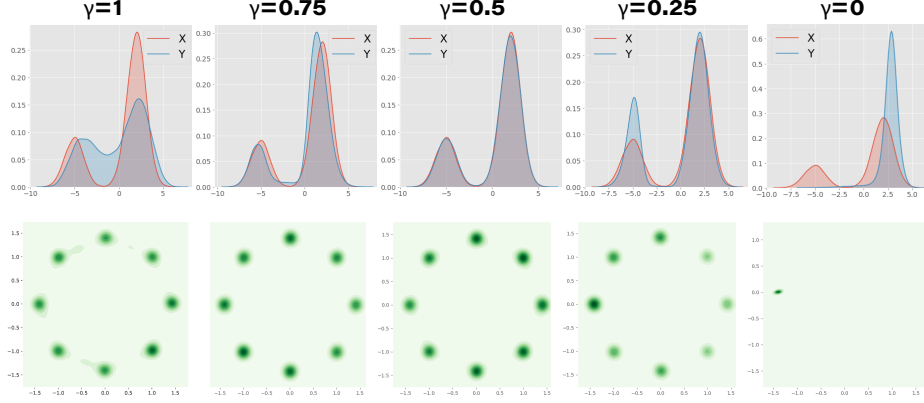


Figure 5: Fitting 1D bi-modal Gaussian (*top*) and 2D 8-Gaussian mixture (*bottom*) by interpolating between the forward ACT ($\gamma = 1$) and backward ACT ($\gamma = 0$).

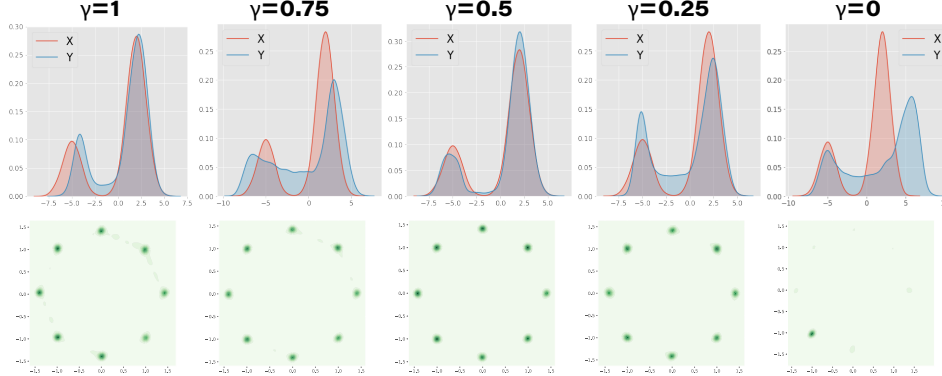


Figure 6: Fitting 1D bi-modal Gaussian (*top*) and 2D 8-Gaussian mixture (*bottom*) by interpolating between the forward ACT ($\gamma = 1$) and backward ACT ($\gamma = 0$), equipped with critic \mathcal{T}_η .

transport cost only encourages mode seeking/dropping behaviors; by contrast, combining both costs provides a user-controllable balance between mode covering and seeking, leading to satisfactory fitting performance, as shown in columns 2 to 4. Note that for a fair comparison, we stop the fitting at the same iteration; in practice, we find if training with more iterations, both $\gamma = 0.75$ and $\gamma = 0.25$ can achieve comparable results as $\gamma = 0.5$. Allowing the mode covering and seeking behaviors to be controlled by tuning γ is an attractive property of ACT_γ .

3.3 Adversarial ACT cost

Adversarial ACT for toy data: We also investigate the mode covering/seeking behaviors when ACT is equipped with a critic. In this setting, the cost is now calculated with the output of the critic, and we optimize the critic by maximizing the ACT cost. We keep the setting the same as the case without the critic and explore the mode covering/seeking behavior by adjusting the coefficient γ , as shown in Fig. 6. We can observe that with the help of the co-adapted critic, the fitting results become less susceptible to pure mode covering or seeking behaviors, especially for $\gamma = 1$ and $\gamma = 0$, and setting $\gamma = 0.5$ that balances the forward and backward CT costs remain the best choice. To further illustrate the properties of adversarial ACT, we have conducted related experiments on Stack-MNIST, whose details are deferred to Appendix B.3.

Table 1: Comparison of generative models on CIFAR-10, CelebA and LSUN. (Top-3 are in bold; IS stands for Inception Score)

Method	Fréchet Inception Distance (FID, ↓)			IS (↑)
	CIFAR-10	CelebA	LSUN-bedroom	CIFAR-10
WGAN [Arjovsky et al., 2017]	51.3±1.5	37.1±1.9	73.3±2.5	6.9±0.1
WGAN-GP [Gulrajani et al., 2017]	19.0±0.8	18.0±0.7	26.9±1.1	7.9±0.1
SN-SMMDGAN [Arbel et al., 2018]	25.0±0.3	12.4±0.2	-	7.3±0.1
Cramér-GAN [Bellemare et al., 2017]	40.3±0.2	31.3±0.2	54.2±0.4	6.4±0.1
CTGAN [Wei et al., 2018]	17.6±0.7	15.8±0.6	19.5±1.2	5.1±0.1
OT-GAN [Salimans et al., 2018]	32.5±0.6	19.4±3.0	70.5±5.3	8.5±0.1
SWG [Deshpande et al., 2018]	33.7±1.5	21.9±2.0	67.9±2.7	-
Max-SWG [Deshpande et al., 2019]	23.6±0.5	10.1±0.6	40.1±4.5	-
SWGAN [Wu et al., 2019]	17.0±1.0	13.2±0.7	14.9±1.0	-
DCGAN [Radford et al., 2015]	30.2±0.9	52.5±2.2	61.7±2.9	6.2±0.1
ACT-DCGAN	22.1±1.1	29.4±2.0	32.6±2.5	7.5±0.1
SNGAN [Miyato et al., 2018]	21.5±1.3	21.7±1.5	31.1±2.1	8.2±0.1
ACT-SNGAN	17.2±1.0	9.2±1.0	16.8±2.1	8.8±0.1



Figure 7: Generated samples of the deep generative model that adopts the backbone of SNGAN but is optimized with the ACT cost on CIFAR-10, CelebA, and LSUN-Bedroom. See Appendix B for more results.

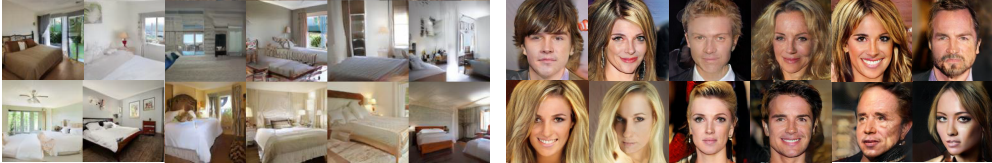


Figure 8: Analogous plot to Fig. 7 for *Left*: LSUN-Bedroom (128x128) and *Right*: CelebA-HQ (256x256).

Adversarial ACT for natural images: We conduct a variety of experiments on natural images to evaluate the performance and reveal the properties of DGMs optimized under the ACT cost. We consider three widely-used image datasets, including CIFAR-10 [Krizhevsky et al., 2009], CelebA [Liu et al., 2015], and LSUN-bedroom [Yu et al., 2015], and compare the results of DGMs optimized with the ACT cost against DGMs trained with the vanilla GAN and its various generalizations.

Note different from previous experiments on toy data, where the transport cost $c(\mathbf{x}, \mathbf{y})$ can be defined by directly comparing \mathbf{x} and \mathbf{y} , for natural images, whose differences in raw pixel values are often not that meaningful, we need to compare $\mathcal{T}_\eta(\mathbf{x})$ and $\mathcal{T}_\eta(\mathbf{y})$, where $\mathcal{T}_\eta(\cdot)$ is a critic that plays the role of adversarial feature extraction, as discussed in Section 2.3. In particular, we use (14) to define the transport cost as $c_\eta(\mathbf{x}, \mathbf{y}) = 1 - \cos(\mathcal{T}_\eta(\mathbf{x}), \mathcal{T}_\eta(\mathbf{y}))$ and parameterize the navigators with $d_{\phi, \eta}(\mathbf{x}, \mathbf{y})$ defined in (15). We test with the architecture suggested in Radford et al. [2015] as a standard CNN backbone and also apply the architecture in Miyato et al. [2018] as the ResNet [He et al., 2016] backbone. Specifically, we use the same architecture for the generator, and slightly modify the output dimension of the discriminator architecture as 2048 for \mathcal{T}_η of the critic. We train this model with (16) and (13), and to keep close to the corresponding backbone’s original experiment setting, we set $N = M = 64$ for all experiments.

We summarize in Table 1 the Fréchet inception distance (FID) of Heusel et al. [2017] on all datasets and Inception Score (IS) of Salimans et al. [2016] on CIFAR-10. Both FID and IS are calculated using a pre-trained inception model [Szegedy et al., 2016]. Lower FID and higher IS scores indicate better image quality. We observe that ACT-DCGAN and ACT-SNGAN, which are DCGAN and SNGAN backbones optimized with the ACT cost, convincingly outperform DCGAN and SNGAN, respectively, suggesting that ACT is compatible with standard GANs and WGANs and generally helps improve generation quality. Moreover, ranked among the Top 3 on all datasets, ACT-SNGAN performs on par with the best benchmarks on CIFAR-10 and CelebA, while slightly worse on LSUN. The qualitative results shown in Fig. 7 are consistent with quantitative results in Table 1. To additionally show how ACT works for more complex generation tasks, we show in Fig. 8 example higher-resolution images generated by ACT-SNGAN on LSUN bedroom and CelebA-HQ.

Note ACT brings consistent improvement to DCGAN and SNGAN by neither improving their network architectures nor gradient regularization. Thus it has great potential to work in conjunction with other state-of-the-art architectures or methods, such as BigGAN [Brock et al., 2018], self-attention GANs [Zhang et al., 2019], BigBiGAN [Donahue and Simonyan, 2019], progressive training [Karras et al., 2018], self-supervised learning [Chen et al., 2019], and data augmentation [Karras et al., 2020, Zhao et al., 2020a,b], which we leave for future study. As the paper is primarily focused on constructing and validating a new approach to measure the difference between two probability distributions, we have focused on demonstrating the efficacy of the proposed CT/ACT on toy data and benchmark image data with moderate resolutions. We have focused on adapting DCGAN and SNGAN under ACT, and we leave to future work using the ACT to optimize a big DGM, such as BigGAN, that is often trained for high-resolution images with a substantially bigger network and larger mini-batch size and hence requires intensive computation that is not easy to afford.

4 Conclusion

We propose conditional transport (CT) as a new divergence to measure the difference between two probability distributions, via the use of both forward-path and backward-path point-to-point conditional distributions. To apply CT to two distributions that have unknown density functions but are easy to sample from, we introduce the amortized CT (ACT) cost whose estimation only requires access to empirical samples. ACT amortizes the computation of its conditional transport plans via its navigators, removing the need of a separate iterative procedure for each mini-batch, and provides unbiased mini-batch based sample gradients that are simple to compute. Its minimization, achieved with the collaboration between the generator, forward navigator, and backward navigator, is shown to be robust to the mini-batch size. In addition, empirical analysis suggests the combination weight of the forward and backward CT costs can be adjusted to encourage either mode covering or seeking behaviors. We further show that a critic can be integrated into both the point-to-point transport cost of ACT and the feature space of the navigators, adversarially extracting the features from high-dimensional data without biasing the sample gradients. We apply ACT to train both a vanilla GAN and a Wasserstein GAN, by substituting their corresponding statistical distance with the ACT cost. Consistent improvement is observed in our experiments, which shows the potential of the ACT cost in more broader settings where quantifying the difference between distributions plays an important role.

References

- Michael Arbel, Dougal J Sutherland, Mikołaj Bińkowski, and Arthur Gretton. On gradient regularizers for mmd gans. In *Proceedings of the 32nd International Conference on Neural Information Processing Systems*, pages 6701–6711, 2018.
- Martin Arjovsky, Soumith Chintala, and Léon Bottou. Wasserstein generative adversarial networks. In *Proceedings of the 34th International Conference on Machine Learning-Volume 70*, pages 214–223, 2017.
- Yogesh Balaji, Hamed Hassani, Rama Chellappa, and Soheil Feizi. Entropic GANs meet VAEs: A statistical approach to compute sample likelihoods in GANs. In *International Conference on Machine Learning*, pages 414–423, 2019.

- Marc G Bellemare, Ivo Danihelka, Will Dabney, Shakir Mohamed, Balaji Lakshminarayanan, Stephan Hoyer, and Rémi Munos. The Cramer distance as a solution to biased Wasserstein gradients. *arXiv preprint arXiv:1705.10743*, 2017.
- Espen Bernton, Pierre E Jacob, Mathieu Gerber, and Christian P Robert. On parameter estimation with the Wasserstein distance. *Information and Inference: A Journal of the IMA*, 8(4):657–676, 2019.
- Christopher M Bishop. *Pattern Recognition and Machine Learning*. springer, 2006.
- Mikołaj Bińkowski, Dougal J. Sutherland, Michael Arbel, and Arthur Gretton. Demystifying MMD GANs. In *International Conference on Learning Representations*, 2018. URL <https://openreview.net/forum?id=r1lU0zWCW>.
- David M Blei, Alp Kucukelbir, and Jon D McAuliffe. Variational inference: A review for statisticians. *Journal of the American statistical Association*, 112(518):859–877, 2017.
- Leon Bottou, Martin Arjovsky, David Lopez-Paz, and Maxime Oquab. Geometrical insights for implicit generative modeling. *arXiv preprint arXiv:1712.07822*, 2017.
- Andrew Brock, Jeff Donahue, and Karen Simonyan. Large scale GAN training for high fidelity natural image synthesis. *arXiv preprint arXiv:1809.11096*, 2018.
- Ting Chen, Xiaohua Zhai, Marvin Ritter, Mario Lucic, and Neil Houlsby. Self-supervised GANs via auxiliary rotation loss. In *Proceedings of the IEEE Conference on Computer Vision and Pattern Recognition*, pages 12154–12163, 2019.
- Thomas M Cover. *Elements of Information Theory*. John Wiley & Sons, 1999.
- Marco Cuturi. Sinkhorn distances: Lightspeed computation of optimal transport. In *Advances in Neural Information Processing Systems*, pages 2292–2300, 2013.
- Ishan Deshpande, Ziyu Zhang, and Alexander G Schwing. Generative modeling using the sliced Wasserstein distance. In *Proceedings of the IEEE conference on computer vision and pattern recognition*, pages 3483–3491, 2018.
- Ishan Deshpande, Yuan-Ting Hu, Ruoyu Sun, Ayis Pyrros, Nasir Siddiqui, Sanmi Koyejo, Zhizhen Zhao, David Forsyth, and Alexander G Schwing. Max-sliced Wasserstein distance and its use for GANs. In *Proceedings of the IEEE conference on computer vision and pattern recognition*, pages 10648–10656, 2019.
- Adji B Dieng, Francisco JR Ruiz, David M Blei, and Michalis K Titsias. Prescribed generative adversarial networks. *arXiv preprint arXiv:1910.04302*, 2019.
- Jeff Donahue and Karen Simonyan. Large scale adversarial representation learning. In *Advances in Neural Information Processing Systems*, pages 10542–10552, 2019.
- Aude Genevay, Marco Cuturi, Gabriel Peyré, and Francis Bach. Stochastic optimization for large-scale optimal transport. In *Advances in Neural Information Processing Systems*, pages 3440–3448, 2016.
- Aude Genevay, Gabriel Peyré, and Marco Cuturi. Learning generative models with Sinkhorn divergences. In *International Conference on Artificial Intelligence and Statistics*, pages 1608–1617, 2018.
- Ian Goodfellow, Jean Pouget-Abadie, Mehdi Mirza, Bing Xu, David Warde-Farley, Sherjil Ozair, Aaron Courville, and Yoshua Bengio. Generative adversarial nets. In *Advances in Neural Information Processing Systems*, pages 2672–2680, 2014.
- Ishaan Gulrajani, Faruk Ahmed, Martin Arjovsky, Vincent Dumoulin, and Aaron C Courville. Improved training of Wasserstein GANs. In *Advances in Neural Information Processing Systems*, pages 5767–5777, 2017.
- Kaiming He, Xiangyu Zhang, Shaoqing Ren, and Jian Sun. Deep residual learning for image recognition. In *Proceedings of the IEEE conference on computer vision and pattern recognition*, pages 770–778, 2016.

- Martin Heusel, Hubert Ramsauer, Thomas Unterthiner, Bernhard Nessler, and Sepp Hochreiter. GANs trained by a two time-scale update rule converge to a local Nash equilibrium. In *Advances in Neural Information Processing Systems*, pages 6626–6637, 2017.
- Matthew D Hoffman, David M Blei, Chong Wang, and John Paisley. Stochastic variational inference. *The Journal of Machine Learning Research*, 14(1):1303–1347, 2013.
- Ferenc Huszár. Variational inference using implicit distributions. *arXiv preprint arXiv:1702.08235*, 2017.
- Leonid V Kantorovich. On the translocation of masses. *Journal of Mathematical Sciences*, 133(4):1381–1382, 2006.
- Tero Karras, Timo Aila, Samuli Laine, and Jaakko Lehtinen. Progressive growing of GANs for improved quality, stability, and variation. In *International Conference on Learning Representations*, 2018.
- Tero Karras, Miika Aittala, Janne Hellsten, Samuli Laine, Jaakko Lehtinen, and Timo Aila. Training generative adversarial networks with limited data. *arXiv preprint arXiv:2006.06676*, 2020.
- Diederik P. Kingma and Jimmy Ba. Adam: A method for stochastic optimization. In Yoshua Bengio and Yann LeCun, editors, *3rd International Conference on Learning Representations, ICLR 2015, San Diego, CA, USA, May 7-9, 2015, Conference Track Proceedings*, 2015. URL <http://arxiv.org/abs/1412.6980>.
- Diederik P Kingma and Max Welling. Auto-encoding variational Bayes. *arXiv preprint arXiv:1312.6114*, 2013.
- Alex Krizhevsky et al. Learning multiple layers of features from tiny images. 2009.
- Solomon Kullback and Richard A Leibler. On information and sufficiency. *The Annals of Mathematical Statistics*, 22(1):79–86, 1951.
- Y. Lecun, L. Bottou, Y. Bengio, and P. Haffner. Gradient-based learning applied to document recognition. *Proceedings of the IEEE*, 86(11):2278–2324, Nov 1998. ISSN 0018-9219. doi: 10.1109/5.726791.
- Chun-Liang Li, Wei-Cheng Chang, Yu Cheng, Yiming Yang, and Barnabás Póczos. MMD GAN: Towards deeper understanding of moment matching network. In *Advances in Neural Information Processing Systems*, pages 2203–2213, 2017.
- Yujia Li, Kevin Swersky, and Rich Zemel. Generative moment matching networks. In *International Conference on Machine Learning*, pages 1718–1727, 2015.
- Jianhua Lin. Divergence measures based on the Shannon entropy. *IEEE Transactions on Information theory*, 37(1):145–151, 1991.
- Zinan Lin, Ashish Khetan, Giulia Fanti, and Sewoong Oh. Pacgan: The power of two samples in generative adversarial networks. In *Advances in Neural Information Processing Systems*, pages 1498–1507, 2018.
- Ziwei Liu, Ping Luo, Xiaogang Wang, and Xiaoou Tang. Deep learning face attributes in the wild. In *Proceedings of the IEEE international conference on computer vision*, pages 3730–3738, 2015.
- Takeru Miyato, Toshiki Kataoka, Masanori Koyama, and Yuichi Yoshida. Spectral normalization for generative adversarial networks. In *International Conference on Learning Representations*, 2018.
- Shakir Mohamed and Balaji Lakshminarayanan. Learning in implicit generative models. *arXiv preprint arXiv:1610.03483*, 2016.
- Kevin P Murphy. *Machine Learning: A Probabilistic Perspective*. MIT Press, 2012.
- Gabriel Peyré and Marco Cuturi. Computational optimal transport. *Foundations and Trends in Machine Learning*, 11(5-6):355–607, 2019.

- Alec Radford, Luke Metz, and Soumith Chintala. Unsupervised representation learning with deep convolutional generative adversarial networks. *arXiv preprint arXiv:1511.06434*, 2015.
- Tim Salimans, Ian Goodfellow, Wojciech Zaremba, Vicki Cheung, Alec Radford, and Xi Chen. Improved techniques for training GANs. In *Advances in Neural Information Processing Systems*, pages 2234–2242, 2016.
- Tim Salimans, Han Zhang, Alec Radford, and Dimitris Metaxas. Improving GANs using optimal transport. *arXiv preprint arXiv:1803.05573*, 2018.
- Filippo Santambrogio. *Optimal Transport for Applied Mathematicians: Calculus of Variations, PDEs, and Modeling*, volume 87. Birkhäuser, 2015.
- Akash Srivastava, Lazar Valkov, Chris Russell, Michael U Gutmann, and Charles Sutton. Veegan: Reducing mode collapse in gans using implicit variational learning. In *Advances in neural information processing systems*, pages 3308–3318, 2017.
- Christian Szegedy, Vincent Vanhoucke, Sergey Ioffe, Jon Shlens, and Zbigniew Wojna. Rethinking the inception architecture for computer vision. In *Proceedings of the IEEE conference on computer vision and pattern recognition*, pages 2818–2826, 2016.
- Dustin Tran, Rajesh Ranganath, and David Blei. Hierarchical implicit models and likelihood-free variational inference. In *Advances in Neural Information Processing Systems*, pages 5523–5533, 2017.
- Cédric Villani. *Optimal Transport: Old and New*, volume 338. Springer Science & Business Media, 2008.
- Martin J Wainwright and Michael Irwin Jordan. *Graphical models, exponential families, and variational inference*. Now Publishers Inc, 2008.
- Xiang Wei, Boqing Gong, Zixia Liu, Wei Lu, and Liqiang Wang. Improving the improved training of Wasserstein GANs: A consistency term and its dual effect. In *International Conference on Learning Representations*, 2018.
- Jiqing Wu, Zhiwu Huang, Dinesh Acharya, Wen Li, Janine Thoma, Danda Pani Paudel, and Luc Van Gool. Sliced Wasserstein generative models. In *Proceedings of the IEEE conference on computer vision and pattern recognition*, pages 3713–3722, 2019.
- Yujia Xie, Xiangfeng Wang, Ruijia Wang, and Hongyuan Zha. A fast proximal point method for computing exact Wasserstein distance. In *Uncertainty in Artificial Intelligence*, pages 433–453. PMLR, 2020.
- Mingzhang Yin and Mingyuan Zhou. Semi-implicit variational inference. In *International Conference on Machine Learning*, pages 5660–5669, 2018.
- Fisher Yu, Ari Seff, Yinda Zhang, Shuran Song, Thomas Funkhouser, and Jianxiong Xiao. LSUN: Construction of a large-scale image dataset using deep learning with humans in the loop. *arXiv preprint arXiv:1506.03365*, 2015.
- Han Zhang, Ian Goodfellow, Dimitris Metaxas, and Augustus Odena. Self-attention generative adversarial networks. In *International Conference on Machine Learning*, pages 7354–7363. PMLR, 2019.
- Richard Zhang, Phillip Isola, Alexei A Efros, Eli Shechtman, and Oliver Wang. The unreasonable effectiveness of deep features as a perceptual metric. In *CVPR*, 2018.
- Shengyu Zhao, Zhijian Liu, Ji Lin, Jun-Yan Zhu, and Song Han. Differentiable augmentation for data-efficient GAN training. *arXiv preprint arXiv:2006.10738*, 2020a.
- Zhengli Zhao, Zizhao Zhang, Ting Chen, Sameer Singh, and Han Zhang. Image augmentations for GAN training. *arXiv preprint arXiv:2006.02595*, 2020b.

Comparing Probability Distributions with Conditional Transport: Appendix

A Proofs

Proof of Lemma 1. If $\mathbf{y} \sim p_\theta(\mathbf{y})$ is equal to $\mathbf{x} \sim p_X(\mathbf{x})$ in distribution, then $p_X(\mathbf{x}) = p_\theta(\mathbf{x})$ for any $\mathbf{x} \in \mathbb{R}^V$. For (2) we have $\int p_X(\mathbf{x})\pi_\phi(\mathbf{y}|\mathbf{x})d\mathbf{y} = p_X(\mathbf{x}) \int \pi_\phi(\mathbf{y}|\mathbf{x})d\mathbf{y} = p_X(\mathbf{x})$ and

$$\begin{aligned} \int p_X(\mathbf{x})\pi_\phi(\mathbf{y}|\mathbf{x})d\mathbf{x} &= \int p_X(\mathbf{x}) \frac{e^{-d_\phi(\mathbf{x},\mathbf{y})}p_\theta(\mathbf{y})}{\int e^{-d_\phi(\mathbf{x},\mathbf{y})}p_\theta(\mathbf{y})d\mathbf{y}}d\mathbf{x} \\ &= p_\theta(\mathbf{y}) \int \frac{e^{-d_\phi(\mathbf{x},\mathbf{y})}p_X(\mathbf{x})}{\int e^{-d_\phi(\mathbf{x},\mathbf{y})}p_\theta(\mathbf{y})d\mathbf{y}}d\mathbf{x}. \end{aligned}$$

If $e^{-d_\phi(\mathbf{x},\mathbf{y})} = \mathbf{1}(\mathbf{x} = \mathbf{y})$, then we further have

$$\int \frac{e^{-d_\phi(\mathbf{x},\mathbf{y})}p_X(\mathbf{x})}{\int e^{-d_\phi(\mathbf{x},\mathbf{y})}p_\theta(\mathbf{y})d\mathbf{y}}d\mathbf{x} = \int \frac{\mathbf{1}(\mathbf{x} = \mathbf{y})p_X(\mathbf{x})}{\int \mathbf{1}(\mathbf{x} = \mathbf{y})p_\theta(\mathbf{y})d\mathbf{y}}d\mathbf{x} = \int \mathbf{1}(\mathbf{x} = \mathbf{y}) \frac{p_X(\mathbf{x})}{p_\theta(\mathbf{x})}d\mathbf{x} = 1$$

and hence it is true that

$$\int p_X(\mathbf{x})\pi_\phi(\mathbf{y}|\mathbf{x})d\mathbf{x} = p_\theta(\mathbf{y}).$$

Similarly, for (3) we have $\int p_\theta(\mathbf{y})\pi_\phi(\mathbf{x}|\mathbf{y})d\mathbf{x} = p_\theta(\mathbf{y})$ and can prove $\int p_\theta(\mathbf{y})\pi_\phi(\mathbf{x}|\mathbf{y})d\mathbf{y} = p_X(\mathbf{x})$ given these two conditions. \square

Proof of Lemma 2. Since $c(\mathbf{x}, \mathbf{y}) \geq 0$ by definition, we have $\mathcal{C}_{\phi,\theta}(\mu \rightarrow \nu) \geq 0$ and $\mathcal{C}_{\phi,\theta}(\mu \leftarrow \nu) \geq 0$. When $\mu = \nu$, it is known that $\mathcal{W}(\mu, \nu) = 0$. If $\mathbf{y} \sim p_\theta(\mathbf{y})$ is equal to $\mathbf{x} \sim p_X(\mathbf{x})$ in distribution, which means $p_X(\mathbf{x}) = p_\theta(\mathbf{x})$ and $p_X(\mathbf{y}) = p_\theta(\mathbf{y})$ for any $\mathbf{x}, \mathbf{y} \in \mathbb{R}^V$ and $\mu = \nu$, then we have

$$\begin{aligned} \mathcal{C}_{\phi,\theta}(\mu \rightarrow \nu) &= \int \int c(\mathbf{x}, \mathbf{y})p_X(\mathbf{x})\pi_\phi(\mathbf{y}|\mathbf{x})d\mathbf{x}d\mathbf{y} \\ &= \int \int c(\mathbf{x}, \mathbf{y}) \frac{e^{-d_\phi(\mathbf{x},\mathbf{y})}p_X(\mathbf{x})p_\theta(\mathbf{y})}{\int e^{-d_\phi(\mathbf{x},\mathbf{y})}p_\theta(\mathbf{y})d\mathbf{y}}d\mathbf{x}d\mathbf{y} \\ &= \int \int c(\mathbf{y}, \mathbf{x}) \frac{e^{-d_\phi(\mathbf{x},\mathbf{y})}p_X(\mathbf{y})p_\theta(\mathbf{x})}{\int e^{-d_\phi(\mathbf{x},\mathbf{y})}p_\theta(\mathbf{x})d\mathbf{x}}d\mathbf{x}d\mathbf{y} \\ &= \int \int c(\mathbf{y}, \mathbf{x}) \frac{e^{-d_\phi(\mathbf{x},\mathbf{y})}p_\theta(\mathbf{y})p_X(\mathbf{x})}{\int e^{-d_\phi(\mathbf{x},\mathbf{y})}p_X(\mathbf{x})d\mathbf{x}}d\mathbf{x}d\mathbf{y} \\ &= \int \int c(\mathbf{x}, \mathbf{y})p_\theta(\mathbf{y}) \frac{e^{-d_\phi(\mathbf{x},\mathbf{y})}p_X(\mathbf{x})}{\int e^{-d_\phi(\mathbf{x},\mathbf{y})}p_X(\mathbf{x})d\mathbf{x}}d\mathbf{x}d\mathbf{y} \\ &= \int \int c(\mathbf{x}, \mathbf{y})p_\theta(\mathbf{y})\pi_\phi(\mathbf{x}|\mathbf{y})d\mathbf{x}d\mathbf{y} \\ &= \mathcal{C}_{\phi,\theta}(\mu \leftarrow \nu) \end{aligned}$$

and hence $\mathcal{C}_{\phi,\theta}(\mu, \nu) = \mathcal{C}_{\phi,\theta}(\mu \rightarrow \nu) = \mathcal{C}_{\phi,\theta}(\mu \leftarrow \nu) \geq 0 = \mathcal{W}(\mu, \nu)$.

If $e^{-d_\phi(\mathbf{x},\mathbf{y})} = \mathbf{1}(\mathbf{x} = \mathbf{y})$, since $c(\mathbf{x}, \mathbf{x}) = 0$ by definition, we have

$$\begin{aligned} \mathcal{C}_{\phi,\theta}(\mu \rightarrow \nu) &= \int \int c(\mathbf{x}, \mathbf{y}) \frac{\mathbf{1}(\mathbf{x} = \mathbf{y})p_X(\mathbf{x})p_\theta(\mathbf{y})}{\int \mathbf{1}(\mathbf{x} = \mathbf{y})p_\theta(\mathbf{y})d\mathbf{y}}d\mathbf{x}d\mathbf{y} \\ &= \int \int c(\mathbf{x}, \mathbf{y}) \frac{\mathbf{1}(\mathbf{x} = \mathbf{y})p_X(\mathbf{x})p_\theta(\mathbf{y})}{p_\theta(\mathbf{x})}d\mathbf{x}d\mathbf{y} \\ &= \int \int c(\mathbf{x}, \mathbf{y})\mathbf{1}(\mathbf{x} = \mathbf{y})p_\theta(\mathbf{y})d\mathbf{x}d\mathbf{y} \\ &= \int c(\mathbf{x}, \mathbf{x})p_\theta(\mathbf{x})d\mathbf{x} \\ &= 0. \end{aligned}$$

\square

Proof of Lemma 3. According to the strong law of large numbers, when $M \rightarrow \infty$, $\hat{\nu}_M(A) = \frac{1}{M} \sum_{j=1}^M \mathbf{1}(\mathbf{y}_j \in A)$ converges almost surely to

$$\frac{1}{M} \sum_{j=1}^M \mathbb{E}_{\mathbf{y}_j \sim p_{\theta}(\mathbf{y})} [\mathbf{1}(\mathbf{y}_j \in A)] = \int_A p_{\theta}(\mathbf{y}) d\mathbf{y} = \nu(A)$$

and hence $C_{\phi, \theta}(\mu \rightarrow \hat{\nu}_M)$ converges to $C_{\phi, \theta}(\mu \rightarrow \nu)$. Therefore, $\mathbb{E}_{\mathbf{y}_{1:M} \stackrel{iid}{\sim} p_{\theta}(\mathbf{y})} [C_{\phi, \theta}(\mu \rightarrow \hat{\nu}_M)]$ converges to $C_{\phi, \theta}(\mu \rightarrow \nu)$. Similarly, we can prove that as $N \rightarrow \infty$, $\mathbb{E}_{\mathbf{x}_{1:N} \stackrel{iid}{\sim} p_X(\mathbf{x})} [C_{\phi, \theta}(\hat{\mu}_N \leftarrow \nu)]$ converges to $C_{\phi, \theta}(\mu \leftarrow \nu)$. Therefore, $C_{\phi, \theta}(\mu, \nu, N, M)$ defined in (11) converges to $\frac{1}{2} C_{\phi, \theta}(\mu \rightarrow \nu) + \frac{1}{2} C_{\phi, \theta}(\mu \leftarrow \nu) = C_{\phi, \theta}(\mu, \nu)$ as $N, M \rightarrow \infty$. \square

Proof of Lemma 4.

$$\begin{aligned} C_{\phi, \theta}(\mu, \nu, N, M) &= \frac{1}{2} \mathbb{E}_{\mathbf{y}_{1:M} \stackrel{iid}{\sim} p_{\theta}(\mathbf{y})} [C_{\phi, \theta}(\mu \rightarrow \hat{\nu}_M)] + \frac{1}{2} \mathbb{E}_{\mathbf{x}_{1:N} \stackrel{iid}{\sim} p_X(\mathbf{x})} [C_{\phi, \theta}(\hat{\mu}_N \leftarrow \nu)] \\ &= \frac{1}{2} \mathbb{E}_{\mathbf{x} \sim p_X(\mathbf{x}), \mathbf{y}_{1:M} \stackrel{iid}{\sim} p_{\theta}(\mathbf{y})} [C_{\phi, \theta}(\mathbf{x} \rightarrow \hat{\nu}_M)] + \frac{1}{2} \mathbb{E}_{\mathbf{x}_{1:N} \stackrel{iid}{\sim} p_X(\mathbf{x}), \mathbf{y} \sim p_{\theta}(\mathbf{y})} [C_{\phi, \theta}(\hat{\mu}_N \leftarrow \mathbf{y})] \\ &= \frac{1}{2} \mathbb{E}_{\mathbf{x} \sim \hat{p}_N(\mathbf{x})} \mathbb{E}_{\mathbf{x}_{1:M} \stackrel{iid}{\sim} p_X(\mathbf{x}), \mathbf{y}_{1:M} \stackrel{iid}{\sim} p_{\theta}(\mathbf{y})} [C_{\phi, \theta}(\mathbf{x} \rightarrow \hat{\nu}_M)] \\ &\quad + \frac{1}{2} \mathbb{E}_{\mathbf{y} \sim \hat{p}_M(\mathbf{y})} \mathbb{E}_{\mathbf{x}_{1:N} \stackrel{iid}{\sim} p_X(\mathbf{x}), \mathbf{y}_{1:M} \stackrel{iid}{\sim} p_{\theta}(\mathbf{y})} [C_{\phi, \theta}(\hat{\mu}_N \leftarrow \mathbf{y})] \\ &= \mathbb{E}_{\mathbf{x} \sim \hat{p}_N(\mathbf{x}), \mathbf{y} \sim \hat{p}_M(\mathbf{y})} \mathbb{E}_{\mathbf{x}_{1:N} \stackrel{iid}{\sim} p_X(\mathbf{x}), \mathbf{y}_{1:M} \stackrel{iid}{\sim} p_{\theta}(\mathbf{y})} \left[\frac{1}{2} C_{\phi, \theta}(\mathbf{x} \rightarrow \hat{\nu}_M) + \frac{1}{2} C_{\phi, \theta}(\hat{\mu}_N \leftarrow \mathbf{y}) \right]. \quad (18) \end{aligned}$$

Plugging (8) and (9) into the above equation concludes the proof. \square

Proof of Lemma 5. Solving the first expectation of (18), we have

$$\begin{aligned} C_{\phi, \theta}(\mu, \nu, N, M) &= \mathbb{E}_{\mathbf{x}_{1:N} \stackrel{iid}{\sim} p_X(\mathbf{x}), \mathbf{y}_{1:M} \stackrel{iid}{\sim} p_{\theta}(\mathbf{y})} \left[\frac{1}{2N} \sum_{i=1}^N C_{\phi, \theta}(\mathbf{x}_i \rightarrow \hat{\nu}_M) + \frac{1}{2M} \sum_{j=1}^M C_{\phi, \theta}(\hat{\mu}_N \leftarrow \mathbf{y}_j) \right]. \end{aligned}$$

Plugging (8) and (9) into the above equation concludes the proof. \square

B Supplementary Experiment Results

B.1 Additional details for the univariate normal toy example shown in (17)

For the toy example specified in (17), exploiting the normal-normal conjugacy, we have an analytical conditional distribution for the forward navigator as

$$\begin{aligned} \pi_{\phi}(y | x) &\propto e^{-\frac{(x-y)^2}{2e^{\phi}}} \mathcal{N}(y; 0, e^{\theta}) \\ &\propto \mathcal{N}(x; y, e^{\phi}) \mathcal{N}(y; 0, e^{\theta}) \\ &= \mathcal{N}\left(\frac{e^{\theta}}{e^{\theta} + e^{\phi}} x, \frac{e^{\phi} e^{\theta}}{e^{\theta} + e^{\phi}}\right), \end{aligned}$$

and an analytical conditional distribution for the backward navigator as

$$\begin{aligned} \pi_{\phi}(x | y) &\propto e^{-\frac{(x-y)^2}{2e^{\phi}}} \mathcal{N}(x; 0, 1) \\ &\propto \mathcal{N}(y; x, e^{\phi}) \mathcal{N}(x; 0, 1) \\ &= \mathcal{N}\left(\frac{y}{1 + e^{\phi}}, \frac{e^{\phi}}{1 + e^{\phi}}\right). \end{aligned}$$

Plugging them into (2) and (3), respectively, and solving the expectations, we have

$$\begin{aligned} C_{\phi, \theta}(\mu \rightarrow \nu) &= \mathbb{E}_{x \sim \mathcal{N}(0, 1)} \left[\frac{e^{\phi}}{e^{\theta} + e^{\phi}} \left(e^{\theta} + \frac{e^{\phi}}{e^{\theta} + e^{\phi}} x^2 \right) \right] \\ &= \frac{e^{\phi}}{e^{\theta} + e^{\phi}} \left(e^{\theta} + \frac{e^{\phi}}{e^{\theta} + e^{\phi}} \right), \end{aligned}$$

$$\begin{aligned}
C_{\phi, \theta}(\mu \leftarrow \nu) &= \mathbb{E}_{y \sim \mathcal{N}(0, e^\theta)} \left[\frac{e^\phi}{1 + e^\phi} \left(1 + \frac{e^\phi}{1 + e^\phi} y^2 \right) \right] \\
&= \frac{e^\phi}{1 + e^\phi} \left(1 + \frac{e^\phi}{1 + e^\phi} e^\theta \right).
\end{aligned}$$

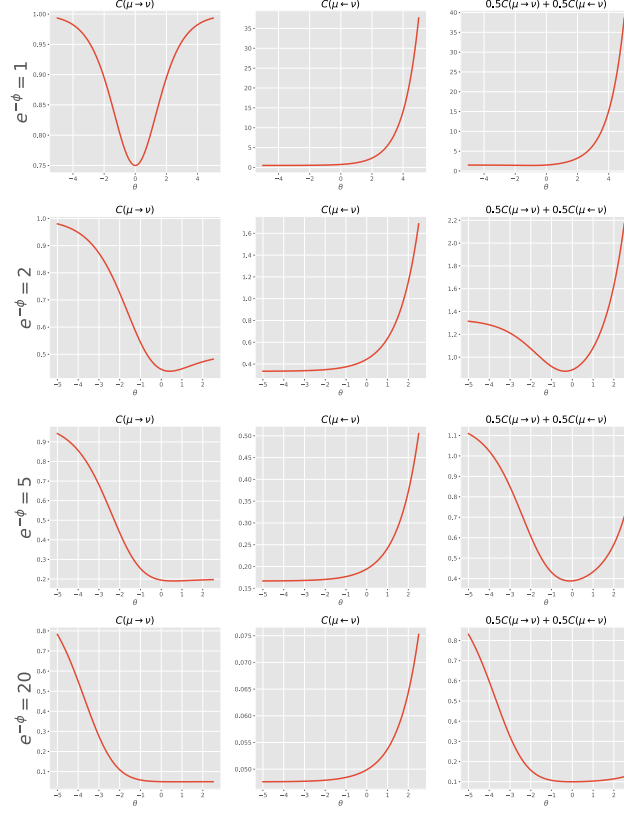


Figure 9: For the univariate normal based toy example specified in (17), we plot the forward, backward, and CT values against θ at four different values of ϕ , which show combining forward and backward balances mode covering and seeking, making it easier for θ to move towards its optimum.

B.2 More results on 2D toy datasets

We visualize the results on the 8-Gaussian mixture and three additional 2D toy datasets. Compared to the 8-Gaussian mixture dataset, the mode collapse issue of both GAN and WGAN-GP becomes more severe on the Swiss-Roll, Half-Moon, and 25-Gaussian datasets, while ACT consistently shows good and stable performance on all of them.

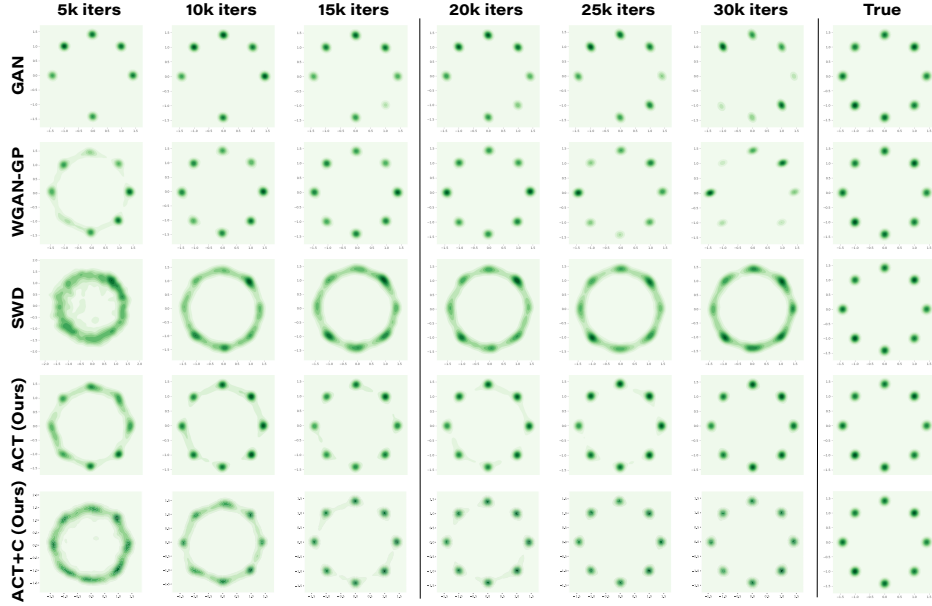


Figure 10: On a 8-Gaussian mixture data, comparison of generation quality and training stability between two mini-max deep generative models (DGMs), including vanilla GAN and Wasserstein GAN with gradient penalty (WGAN-GP), and two mini-max-free DGMs, whose generators are trained under the sliced Wasserstein distance (SWD) and the proposed ACT cost, respectively. The critics of GAN, WGAN-GP, the navigators of ACT and the critics of ACT+C are fixed after 15k iterations. The first column shows the true data density.

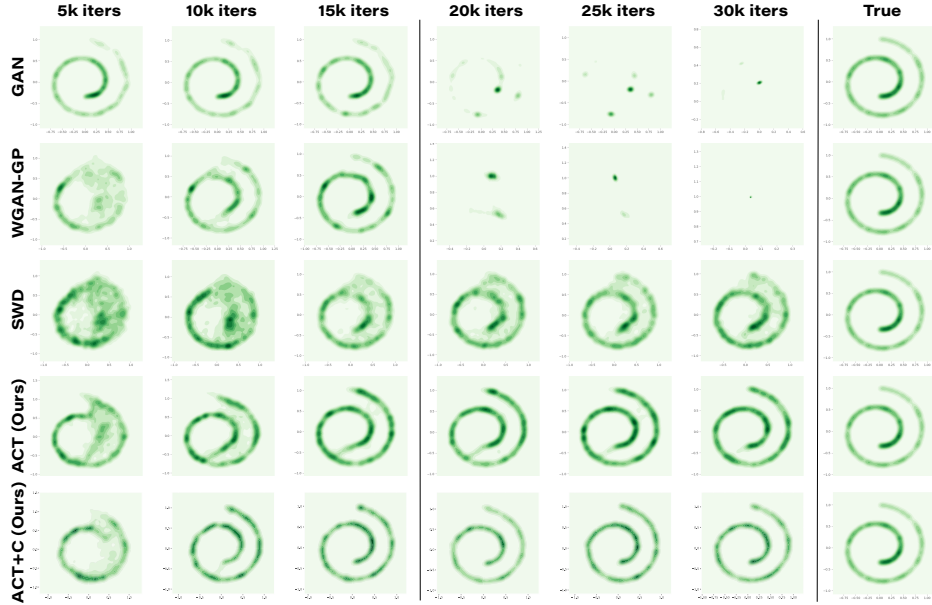


Figure 11: Analogous plot to Fig. 10 for the Swiss-Roll dataset.

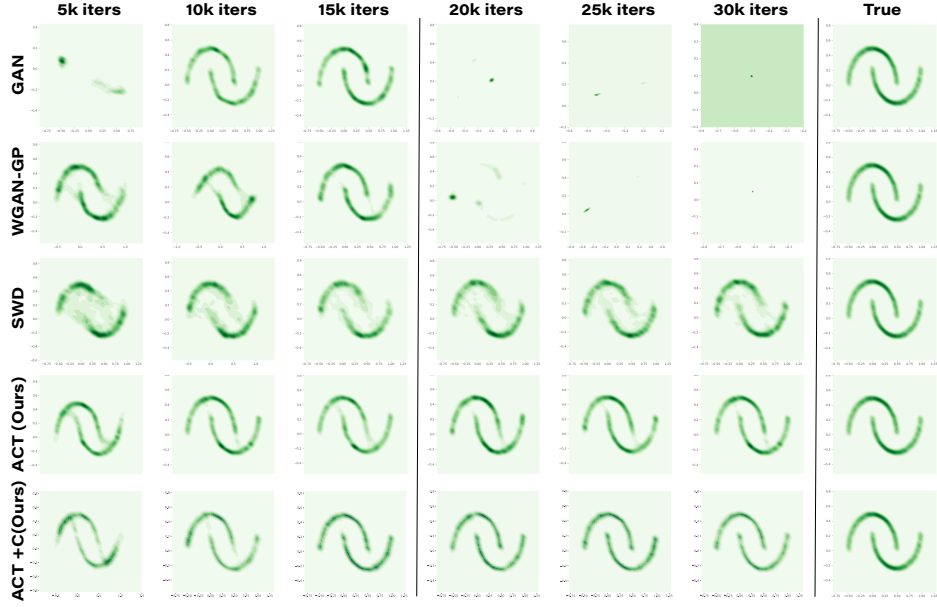


Figure 12: Analogous plot to Fig. 10 for the Half-Moon dataset.

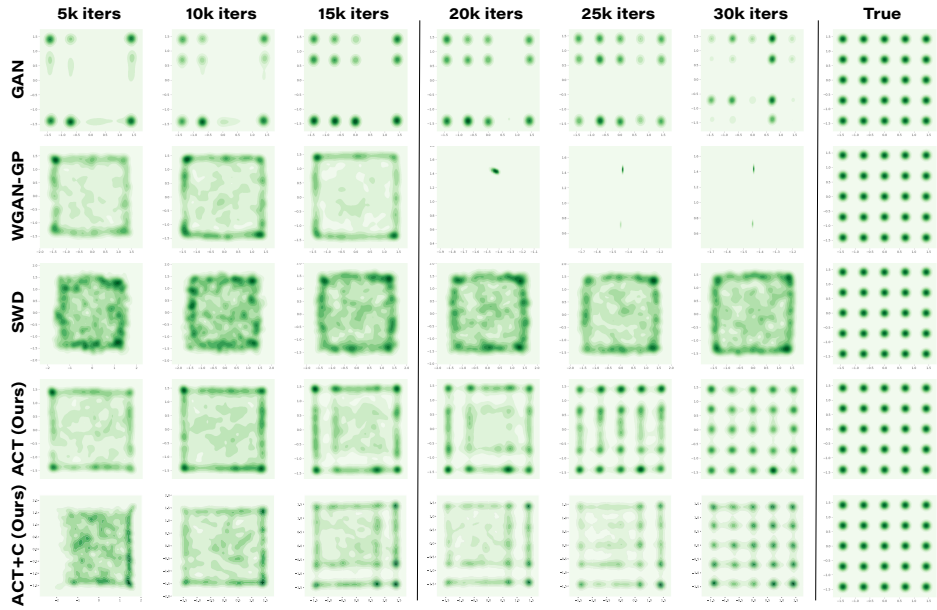


Figure 13: Analogous plot to Fig. 10 for the 25-Gaussian mixture dataset.

We also illustrate the data points and generated samples with empirical samples, shown in Fig. 14. The first column shows the generated samples (marked in blue) and the samples from data distribution (marked in red). To visualize how the feature extractor \mathcal{T}_ϕ used by both navigators works, we set its output dimension as 1 and plot the logits in the third and fifth columns and map the corresponding data (in the second column) and generated samples (in the fourth column) with the same color.

Similarly, we visualize the GAN’s generated samples and logits produced by its discriminator in Fig. 15. We can observe that the discriminator maps the data to very close values. Specifically, in both the 8-Gaussian mixture and 25-Gaussian mixture cases, when the mode collapse occurs, the logits of the missed modes have similar value to the those in the other modes. This property results in GAN’s mode collapse problem and it is commonly observed in GANs. Different from the GAN case, the navigator in our ACT model maps the data with non-saturating logits. We can observe in various multi-mode cases, different modes are assigned with different values by the navigator. This property helps ACT to well resist the mode collapse problem and stabilize the training.

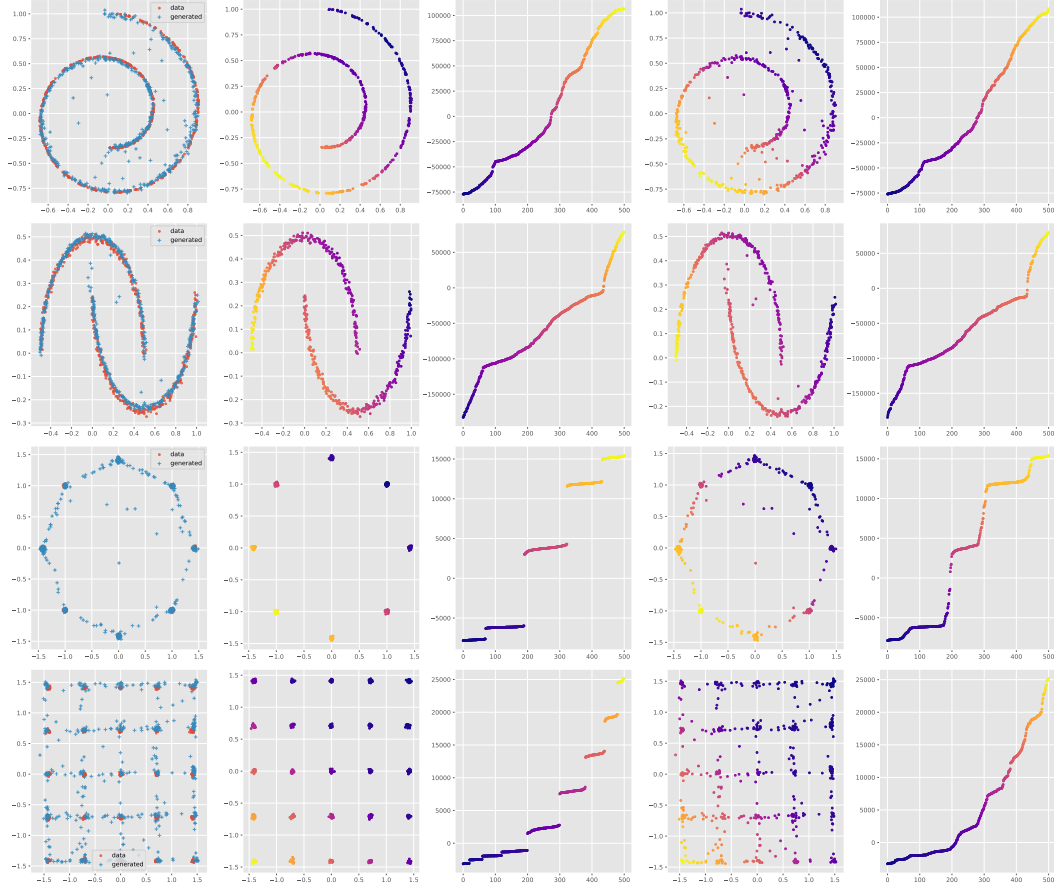


Figure 14: Visual results of *ACT* for generated samples (blue dots) compared to real samples (red dots) on Swiss Roll, Half Moons, 8-Gaussian mixture, and 25-Gaussian mixture. The second and third columns map the data points and their corresponding *navigator* logits by color; The fourth and fifth columns map the generated points and their corresponding *navigator* logits by color.

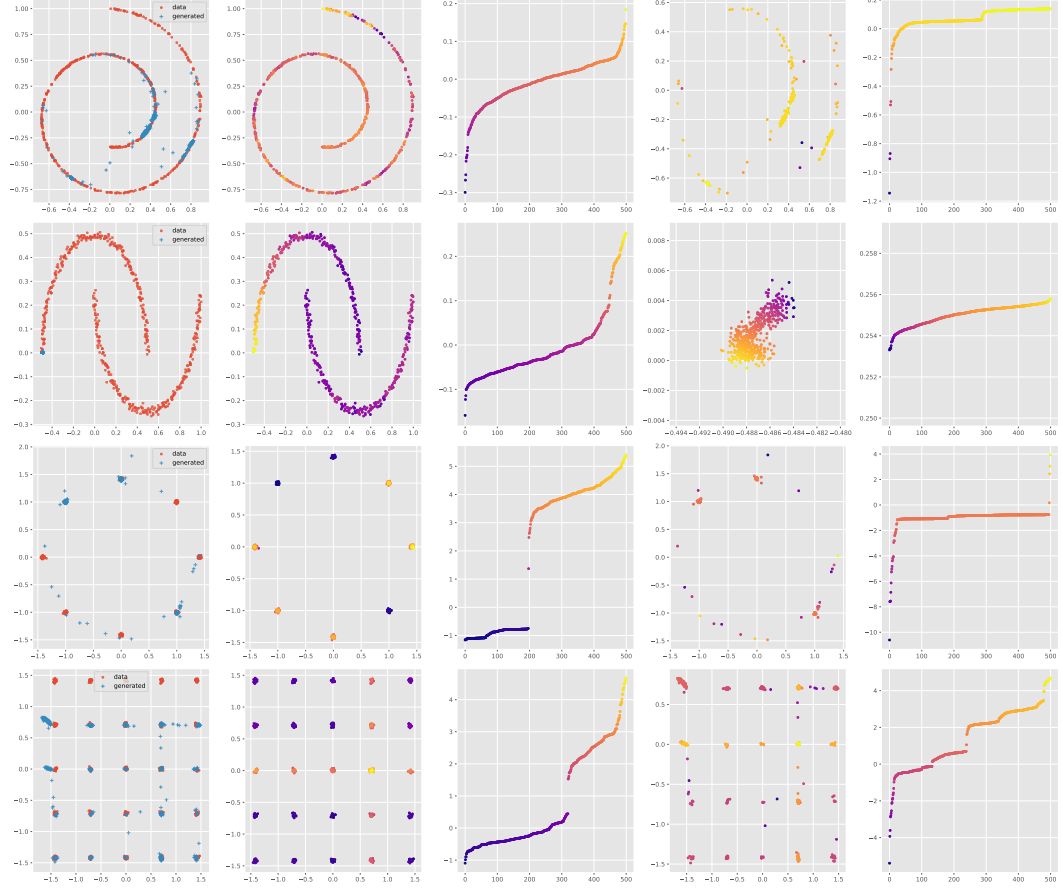


Figure 15: Visual results of *GAN* for generated samples (blue dots) compared to real samples (red dots) on Swiss Roll, Half Moons, 8-Gaussian mixture, and 25-Gaussian mixture. The second and third columns map the data points and their corresponding *discriminator* logits by color; The fourth and fifth columns map the generated points and the corresponding *discriminator* logits by color.

B.3 Results for ablation study

Forward/Backward properties and mode capture The mode covering and mode seeking behaviors discussed in Figs. 5 and 6 also exist in the real image case. For illustration, we use the Stacked-MNIST dataset Srivastava et al. [2017] and fit ACT in three configurations: normal, forward only, and backward only. DCGAN Radford et al. [2015], VEEGAN Srivastava et al. [2017], PacGAN Lin et al. [2018], and PresGAN Dieng et al. [2019] are applied here as the baseline models to evaluate the mode-capturing capability.

Table 2: Assessing mode collapse on Stacked-MNIST. The true total number of modes is 1,000. DCGAN, VEEGAN, and ACT (Backward only) all suffer from collapse. The other models capture nearly all the modes of the data distribution. Furthermore, the distribution of the labels predicted from the images produced by these models is closer to the data distribution, which shows lower KL scores.

Method	Mode Captured	KL
DCGAN Radford et al. [2015]	392.0 ± 7.376	8.012 ± 0.056
VEEGAN Srivastava et al. [2017]	761.8 ± 5.741	2.173 ± 0.045
PacGAN Lin et al. [2018]	992.0 ± 1.673	0.277 ± 0.005
PresGAN Dieng et al. [2019]	999.4 ± 0.80	0.102 ± 0.003
ACT	999.07 ± 0.162	0.181 ± 0.003
ACT (Forward only)	999.18 ± 0.9	0.124 ± 0.003
ACT (Backward only)	192 ± 1.912	9.166 ± 0.06

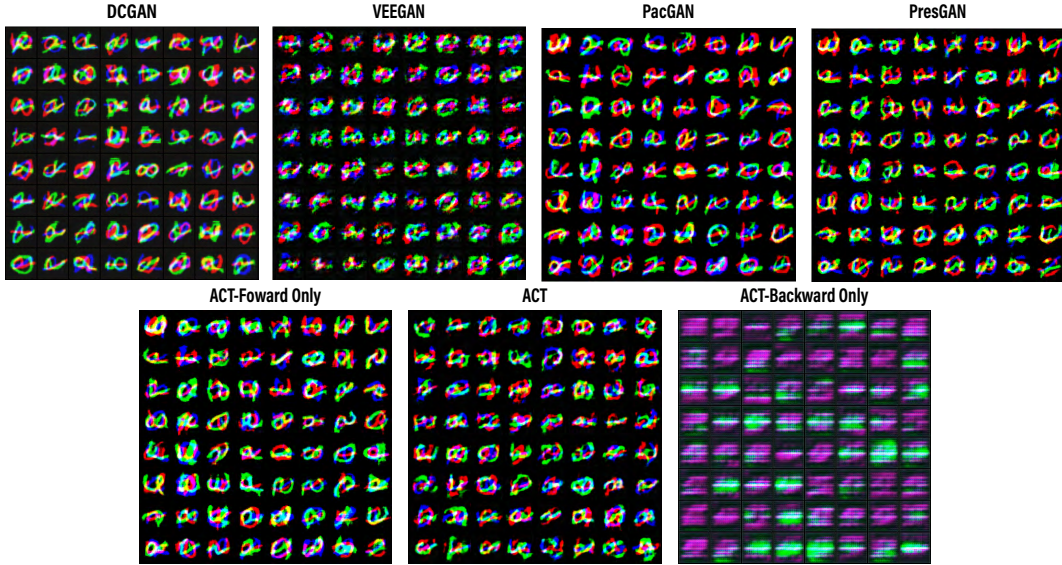


Figure 16: Visual results of the generated samples produced by DCGAN, VEEGAN, PacGAN, PresGAN, and ACT-DCGAN on the Stacked-MNIST dataset.

We calculate the captured mode number of each model, as well as the Kullback–Leibler (KL) divergence of the predicted label distributions between the generated samples and true data samples. For Stacked-MNIST data, there are 1000 modes in total. The results in Table 2 justify ACT using only forward or using both forward and backward can almost capture all the modes, thus we do not suffer from the mode collapse problem. Using backward only can only encourages the mode seeking/dropping behavior. Fig. 16 provides the visual justification of this experiment. Note that in the image case, it is not easy to make the critic be co-adapted with the generator, as shown in the low-dimensional case (Fig. 6). Here if we only apply the backward ACT for optimization, we can still observe the mode seeking behavior of the generator. In more complicated scenarios, *e.g.*, when the dimensionality of the data is much larger than that of Stacked-MNIST, the co-adaptation between the critic and generator becomes more difficult, indicating the necessity of the bi-directional conditional transport.

Transport cost in pixel space *vs.* feature space We visualize the difference of using the transport cost in the pixel space and in the feature space here. In both Figs. 17 and 18, we test with MNSIT and CIFAR-10 data and with the \mathcal{L}_2^2 distance and cosine dissimilarity

as the transport cost, respectively. For the MNIST dataset, due to its simple data structure, ACT can still be trained to generate meaningful digits, though some digits appear blurry. On the CIFAR-10, we can observe the model fails to generate any class of CIFAR images. As the dimensionality of the input space increases, using the distance in the pixel space as transport cost might lose the essential information for the transport and increases the training complexity of the navigator.

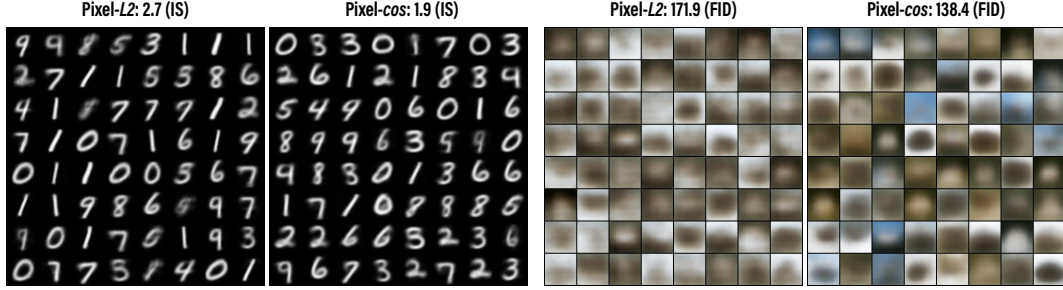


Figure 17: Visual results of generated samples on MNIST and CIFAR-10 using pixel-wise transport cost, with DCGAN (standard CNN) backbone.

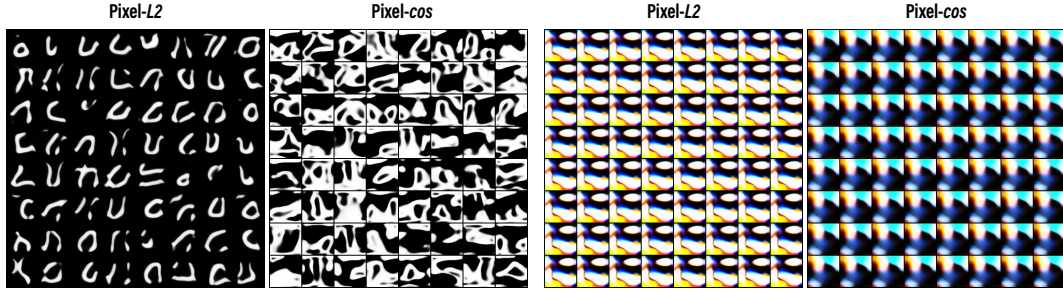


Figure 18: Visual results of generated samples on MNIST and CIFAR-10 using pixel-wise transport cost, with SNGAN (ResNet) backbone. The Inception and FID scores are not shown due to poor visual quality.

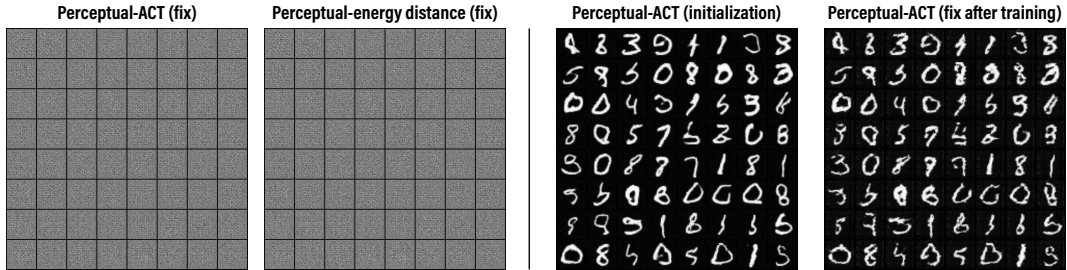


Figure 19: Visual results of generated samples with the perceptual similarity [Zhang et al., 2018] with four different training configurations.

We also consider using the perceptual similarity [Zhang et al., 2018] to define the cost function. Here we test with four configurations: 1) Apply a fixed and pre-trained perceptual loss to calculate the distance between the data and generated samples, use that distance as the point-to-point cost, and calculate ACT to train the generator; 2) Apply a fixed and pre-trained perceptual loss to calculate the energy distance between the data and generated samples to train the generator; 3) Apply the pre-trained perceptual loss as cost and fine-tune with ACT to train the generator; 4) Apply the pre-trained perceptual loss as cost, fine-tune it with ACT to train the generator, and then fix it for 20 more training epochs. We report the visual results of these 4 configurations in Fig.19. As shown, fixing the metric and calculate the distance (either ACT or energy distance) in the feature space does not show good generation results. An explanation could be the pretrained perceptual loss is not trained on the generation task and hence might not be compatible with the learning objective. Thus

Table 3: FID comparison for ACT-DCGAN and ACT-SNGAN on CIFAR-10 with different cost and architecture.

-Standard CNN-		transport cost $c(\mathbf{x}, \mathbf{y})$			
		\mathcal{L}_2^2 -pixel	\cos -pixel	\mathcal{L}_2^2 -feature	\cos -feature
Navigator cost	\mathcal{L}_2^2	171.9	138.4	27.1	24.8
$d(\mathcal{T}_\phi(\mathbf{x}), \mathcal{T}_\phi(\mathbf{y}))$	\cos	157.9	136.2	25.3	25.0
-ResNet-		transport cost $c(\mathbf{x}, \mathbf{y})$			
		\mathcal{L}_2^2 -pixel	\cos -pixel	\mathcal{L}_2^2 -feature	\cos -feature
Navigator cost	\mathcal{L}_2^2	237.2	297.1	22.8	21.6
$d(\mathcal{T}_\phi(\mathbf{x}), \mathcal{T}_\phi(\mathbf{y}))$	\cos	293.1	252.7	19.8	18.0

the cost could not feedback useful signal to guide the generator. Using the energy distance as in Bellemare et al. [2017] shows similar results. We further use the perceptual network as the initialization of our critic \mathcal{T}_η , and train with ACT by maximizing the cost for 40 epochs on MNIST, which produce good-quality generations as shown in the third column. Then we fix the training of this critic and train the generator for 20 more epochs, which lead to degraded generation quality. We expect the generation quality will get worse as the training under the fixed critic continues.

Using alternative cost function We also test ACT with different configurations. As discussed in previous sections, the defined cost may also affect the training of the model. Here we vary the choice of transport cost $c_\eta(\mathbf{x}, \mathbf{y})$ and the navigator cost $d(\mathcal{T}_\phi(\mathbf{x}), \mathcal{T}_\phi(\mathbf{y}))$. For both cost, we test with L_2^2 distance and cosine dissimilarity. Moreover, we also compare the effects of distance in the original pixel space and the feature space (equipped with critic \mathcal{T}_η). The results in Table 3 highlight the importance of the cost in the feature space when dealing with high-dimensional image data. Moreover, compared to the L_2^2 distance, the cosine dissimilarity is observed to improve the model when applied as transport and navigator cost, especially with the ResNet architecture.

Training the critic with the discriminator loss of a vanilla GAN Contrary to the existing critic-based GANs, the sample estimates of ACT cost and its gradient are unbiased regardless of how well the critic is trained. We thus keep the same experiment settings and train the ACT-DCGAN model’s critic with the discriminator loss of standard GANs, *i.e.* $\mathbb{E}_{x \sim \mathbb{P}_d} [-\log(\mathcal{T}_\eta(x))] + \mathbb{E}_{x \sim \mathbb{P}_g} [-\log(1 - \mathcal{T}_\eta(x))]$. The results in Fig. 20 shows that ACT works well in conjunction with the alternative critic training. The quantitative and qualitative on MNIST, CIFAR-10, CelebA, and LSUN are shown in Fig. 20. We can observe the quality of generated samples, while clearly not as good as training the critic with the ACT cost, can still catch up with some of the benchmarks in Table 1.

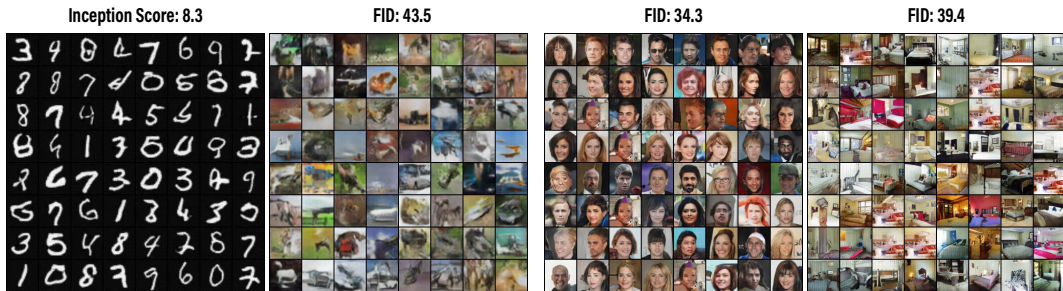


Figure 20: Visual results of using a standard cross-entropy discriminator loss in lieu of ACT cost to train the critic of ACT.

B.4 More results on image datasets

For the experiments on the image datasets, we provide more visual results in this part. Apart from the datasets described in the experiment part, we also test the capacity of single-channel image generation with the MNIST dataset. Considering the inception score and the FID score are designed for RGB natural images, we also calculate the inception score of the real

testing sets for reference. The presented methods are all able to generate meaningful digits on MNIST. If we take a closer look at the digits, the digits generated with \mathcal{L}_2 cost is less natural than the one with cosine cost. Moreover, we show both unconditional and conditional generation results on CIFAR-10. For both unconditional and conditional generation, our proposed method achieves good quantitative and qualitative results.



Figure 21: Unconditional generated samples and inception scores of MNIST, with DCGAN (standard CNN) backbone.

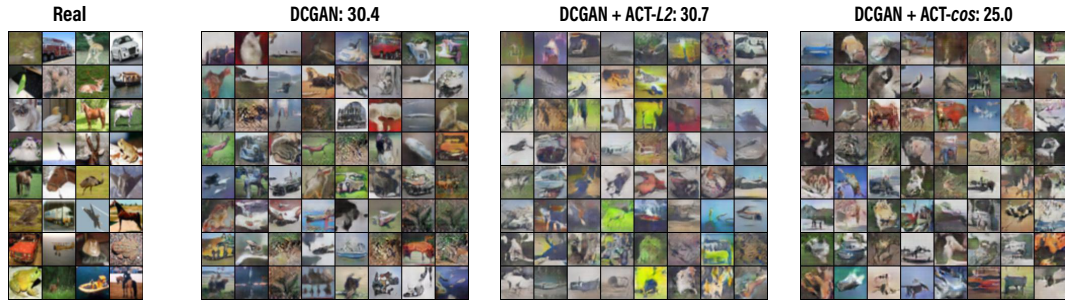


Figure 22: Unconditional generated samples and FIDs of CIFAR-10, with DCGAN (standard CNN) backbone.



Figure 23: Unconditional generated samples and FIDs of CIFAR-10, with SNGAN (ResNet) backbone.

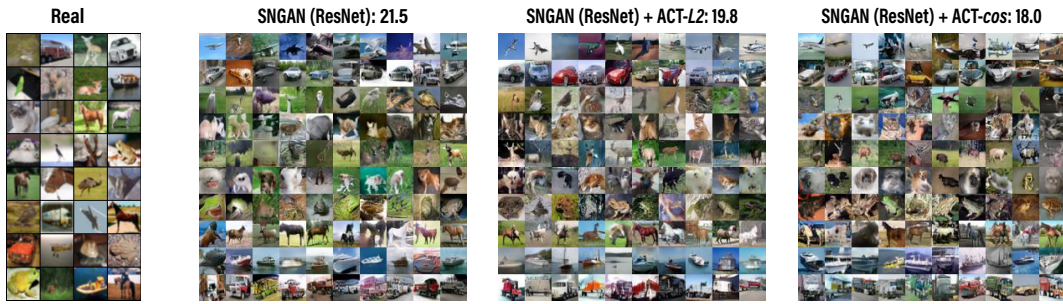


Figure 24: Conditional generated samples and FIDs of CIFAR-10, with SNGAN (ResNet) backbone.

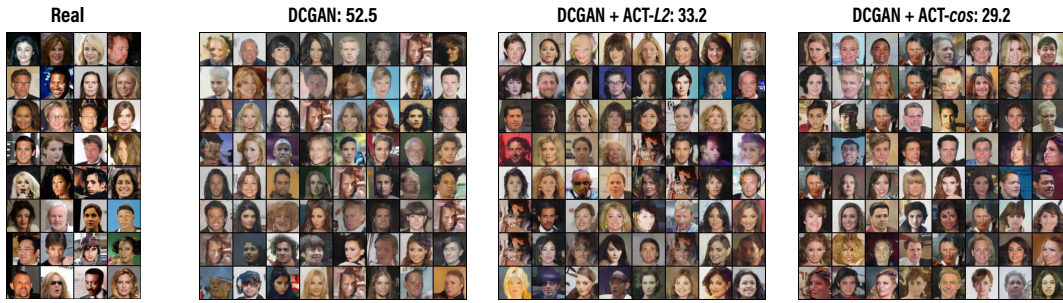


Figure 25: Generated samples and FIDs of CelebA, with DCGAN (standard CNN) backbone.

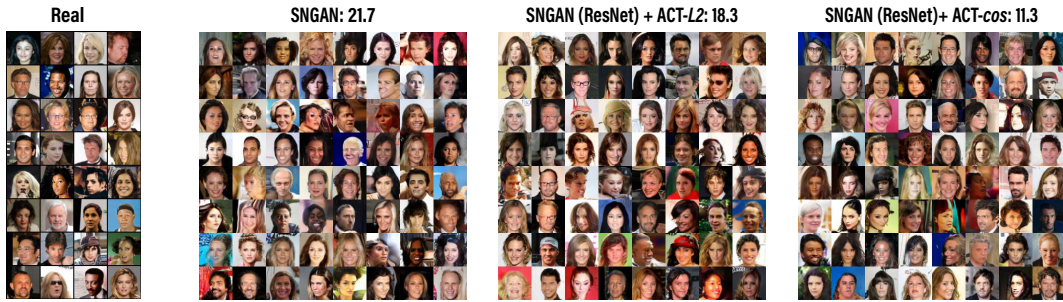


Figure 26: Generated samples and FIDs of CelebA, with SNGAN (ResNet) backbone.

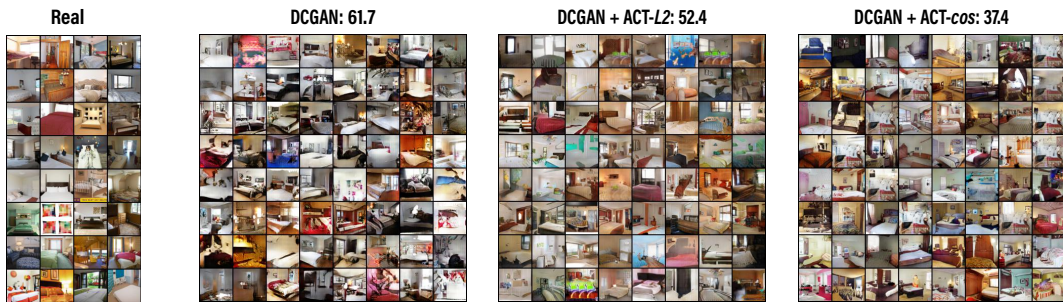


Figure 27: Generated samples and FIDs of LSUN, with DCGAN (standard CNN) backbone.



Figure 28: Generated samples and FIDs of LSUN, with SNGAN (ResNet) backbone.

B.5 Experiment Details

Preparation of datasets We apply the commonly used training set of MNIST (50K gray-scale images, 28×28 pixels) [Lecun et al., 1998], Stacked-MNIST (50K images, 28×28 with 3 channels pixels) [Srivastava et al., 2017], CIFAR-10 (50K color images, 32×32 pixels) [Krizhevsky et al., 2009], CelebA (about 203K color images, resized to 64×64 pixels) [Liu et al., 2015], and LSUN bedrooms (around 3 million color images, resized to 64×64 pixels) [Yu et al., 2015]. The image pixels are normalized to range $[-1, 1]$. For MNIST, when calculate the inception score, we repeat the channel to convert each gray-scale image into a RGB format.

Network architecture and hyperparameters For the network architectures presented here, the slopes of all lReLU functions in the networks are set to 0.1 by default, and the outputs of critic and navigator are normalized with L2 norm. For toy experiments, when training without the critic, the network architecture is shown in Table 5, where we make $H = 100$ and $d = 1$. The navigator is parameterized as $d_\phi(\mathbf{x}, \mathbf{y}) := d_\phi((\mathbf{x} - \mathbf{y}) \circ (\mathbf{x} - \mathbf{y}))$, where \circ denotes the Hadamard product, *i.e.*, the element-wise product. Typically, 10,000 update steps are sufficient. However, our experiments show that the DGM optimized with the ACT cost can be stably trained at least over 500,000 steps (or possibly even more if allowed to running non-stop) regardless of whether the navigators are frozen or not after a certain number of iterations, where the GAN’s discriminator usually diverges long before reaching that many iterations even if we do not freeze it after a certain number of iterations. When adding the critic component, there are two possible parameterizations for $d_{\phi, \eta}(\mathbf{x}, \mathbf{y})$, denoted as “separate” and “joint” strategy (the pseudo-code comparison is shown in Algorithms 1 and 2):

$$\text{Separate: } d_{\phi, \eta}(\mathbf{x}, \mathbf{y}) := 1 - \cos(d_\phi(\mathbf{x}), d_\phi(\mathbf{y}));$$

$$\text{Joint: } d_{\phi, \eta}(\mathbf{x}, \mathbf{y}) := d_\phi((\mathcal{T}_\eta(\mathbf{x}) - \mathcal{T}_\eta(\mathbf{y})) \circ (\mathcal{T}_\eta(\mathbf{x}) - \mathcal{T}_\eta(\mathbf{y}))).$$

For toy experiments, we use the “joint” implementation, where the networks of navigator and critic use the architecture in Table 5, with $H = 100$, $d = 10$ for critic and $H = 100$, $d = 1$ for navigator. On image experiments, we conduct the experiments with both separate and joint implementation. For the separate implementation, we make the navigator and critic as two identical neural networks; in the implementation of the joint one, we make the navigator as a two-layer MLP added on the top of the critic, where the MLP uses architecture shown in Table 5, with $H = 512$, $d = 1$. When the critic network has a large number of parameters, the joint implementation largely reduces the computation complexity and required computation resource like GPU memory. We tested both implementations in the same setting and they are all able to be trained on a single GPU such as NVidia GTX 1080-TI. For image experiments, the comparison between these two implementations is shown in Table 4, where we observe the results are comparable and the joint implementation, with the MLP navigator, shows slightly better performance. A possible explanation is the joint one reduces the training complexity and could be better handled, while the separate one needs more careful fine-tuning. In the toy experiments, we apply the joint strategy and set $H = 10$ and $d = 10$ for the critic, adding a full-connected-layer ($10 \rightarrow 1$) as the navigator. For all image experiments, when applying the separate implementation the output feature dimension of the navigators and that of the critic (*i.e.*, $d_\phi(\cdot), \mathcal{T}_\eta(\cdot) \in \mathbb{R}^m$) are set to $m = 1024$. When applying the implementation B, we apply a critic with the output dimension $m = 1024$ and a MLP with architecture shown in Table 5 ($V = m = 1024$, $H = 512$ and $d = 1$). All models are trained on a single GPU, Nvidia GTX 1080-TI/Nvidia RTX 3090 in our experiments, with 150,000 generator updates (for CIFAR-10 we apply 50,000 iterations).

Table 4: Comparison of different implementation on CIFAR-10, CelebA and LSUN.

Method	Fréchet Inception Distance (FID, ↓)		
	CIFAR-10	CelebA	LSUN-bedroom
ACT-DCGAN (separate)	24.8	29.2	37.4
ACT-DCGAN (joint)	22.1	29.4	32.6
ACT-SNGAN (separate)	18.0	11.3	24.2
ACT-SNGAN (joint)	17.2	9.2	16.8

To keep close to the configuration of the DCGAN and SNGAN experiments setting, we use the the Adam optimizer [Kingma and Ba, 2015] with learning rate $\alpha = 2 \times 10^{-4}$ and $\beta_1 = 0.5$, $\beta_2 = 0.99$ for the parameters of the generator, navigators, and critic. On the DCGAN backbone, we let all the modules update with the same frequency; while on the SNGAN backbone, the critic is updated once per 5 generator updating steps. The performance might be further improved with more careful fine-tuning. For example, the learning rate of the navigator parameter could be made smaller than that of the generator parameter. The true data minibatch size is fixed to $N = 64$ for all experiments. Moreover, with this batch-size we let the generated sample size M the same as minibatch size N for ACT computation and we have monitored the average time for each update step on a single NVidia GTX 1080-TI GPU: On CIFAR-10, each update step takes around 0.1s and 0.2s for DCGAN and SNGAN, respectively; For DCGAN and SNGAN backbone trained with ACT cost each update step takes around 0.4s and 0.7s. On CelebA and LSUN, each update takes 0.6s and 0.7s for DCGAN and SNGAN, respectively; when trained with ACT, the elapsed time for each update increases to at most 3.3s and 3.6s with the separate implementation and 1.4s and 1.8s with the joint implementation, respectively.

Algorithm 1 PyTorch-like style pseudo-code of ACT loss with separate parameterization for $d_{\phi,\eta}(x, y)$.

```
##### Inputs #####
# x: data B x C x W x H;
# y: generated samples B x C x W x H;
# netN: navigator network C x W x H -> d
# netD: critic network C x W x H -> d
# gamma: balance coefficient of forward-backward, default = 0.5

def act_loss(x, y, netN, netD):
    ##### compute cost #####
    f_x = netD(x) # feature of x: B x d
    f_y = netD(y) # feature of y: B x d
    cost = torch.norm(f_x[:,None] - f_y, dim=-1).pow(2) # pairwise cost: B x B

    ##### compute transport map #####
    n_x = netN(x) # feature of x in navigator space: B x d
    n_y = netN(y) # feature of y in navigator space: B x d
    d = pairwise_cosine_similarity(n_x, n_y, dim=-1) - 1 # navigator distance: B x B
    forward_map = torch.softmax(d, dim=1) # forward map is in y wise
    backward_map = torch.softmax(d, dim=0) # backward map is in x wise

    ##### compute ACT loss #####
    # element-wise product of cost and transport map
    act = gamma * (cost * forward_map).sum(1).mean() + (1-gamma) * (cost * backward_map).sum(0).mean()
    return act
```

Algorithm 2 PyTorch-like style pseudo-code of ACT loss with joint parameterization for $d_{\phi,\eta}(x, y)$.

```
##### Inputs #####
# x: data B x C x W x H;
# y: generated samples B x C x W x H;
# netN: navigator network d -> 1
# netD: critic network C x W x H -> d
# gamma: balance coefficient of forward-backward, default = 0.5

def act_loss(x, y, netN, netD):
    ##### compute cost #####
    f_x = netD(x) # feature of x: B x d
    f_y = netD(y) # feature of y: B x d
    cost = torch.norm(f_x[:,None] - f_y, dim=-1).pow(2) # pairwise cost: B x B

    ##### compute transport map #####
    mse_n = (f_x[:,None] - f_y).pow(2) # pairwise mse for navigator network: B x B x d
    d = netN(mse_n).squeeze().mul(-1) # navigator distance: B x B
    forward_map = torch.softmax(d, dim=1) # forward map is in y wise
    backward_map = torch.softmax(d, dim=0) # backward map is in x wise

    ##### compute ACT loss #####
    # element-wise product of cost and transport map
    act = gamma * (cost * forward_map).sum(1).mean() + (1-gamma) * (cost * backward_map).sum(0).mean()
    return act
```

Table 5: Network architecture for toy datasets (V indicates the dimensionality of data).

(a) Generator G_{θ}	(b) Navigator \mathcal{T}_{ϕ} / Discriminator D_{ϕ} / Critic \mathcal{T}_{η}
$\epsilon \in \mathbb{R}^{50} \sim \mathcal{N}(0, 1)$	$\mathbf{x} \in \mathbb{R}^V$
$50 \rightarrow H$, dense, BN, lReLU	$V \rightarrow H$, dense, BN, lReLU
$H \rightarrow \lfloor \frac{H}{2} \rfloor$, dense, BN, lReLU	$H \rightarrow \lfloor \frac{H}{2} \rfloor$, dense, BN, lReLU
$\lfloor \frac{H}{2} \rfloor \rightarrow V$, dense, linear	$\lfloor \frac{H}{2} \rfloor \rightarrow d$, dense, linear

Table 6: DCGAN architecture for the CIFAR-10 dataset ($h = w = 4$).

(a) Generator G_{θ}	(b) Navigator \mathcal{T}_{ϕ} / Critic \mathcal{T}_{η}
$\epsilon \in \mathbb{R}^{128} \sim \mathcal{N}(0, 1)$	$\mathbf{x} \in [-1, 1]^{32 \times 32 \times 3}$
$128 \rightarrow 4 \times 4 \times 512$, dense, linear	3×3 , stride=1 conv 64 lReLU
4×4 , stride=2 deconv. BN 256 ReLU	4×4 , stride=2 conv 64 lReLU
4×4 , stride=2 deconv. BN 128 ReLU	3×3 , stride=1 conv 128 lReLU
4×4 , stride=2 deconv. BN 64 ReLU	4×4 , stride=2 conv 128 lReLU
3×3 , stride=1 conv. 3 Tanh	3×3 , stride=1 conv 256 lReLU
	4×4 , stride=2 conv 256 lReLU
	3×3 , stride=1 conv. 512 lReLU
	$h \times w \times 512 \rightarrow m$, dense, linear

Table 7: DCGAN architecture for the CelebA and LSUN datasets ($h = w = 4$).

(a) Generator G_{θ}	(b) Navigator \mathcal{T}_{ϕ} / Critic \mathcal{T}_{η}
$\epsilon \in \mathbb{R}^{128} \sim \mathcal{N}(0, 1)$	$\mathbf{x} \in [-1, 1]^{64 \times 64 \times 3}$
$128 \rightarrow 4 \times 4 \times 1024$, dense, linear	4×4 , stride=2 conv 64 lReLU
4×4 , stride=2 deconv. BN 512 ReLU	4×4 , stride=2 conv BN 128 lReLU
4×4 , stride=2 deconv. BN 256 ReLU	4×4 , stride=2 conv BN 256 lReLU
4×4 , stride=2 deconv. BN 128 ReLU	3×3 , stride=1 conv BN 512 lReLU
4×4 , stride=2 deconv. BN 64 ReLU	$h \times w \times 512 \rightarrow m$, dense, linear, Normalize
3×3 , stride=1 conv. 3 Tanh	

Table 8: ResNet architecture for the CIFAR-10 dataset.

(a) Generator G_{θ}	(b) Navigator \mathcal{T}_{ϕ} / Critic \mathcal{T}_{η}
$\epsilon \in \mathbb{R}^{128} \sim \mathcal{N}(0, 1)$	$\mathbf{x} \in [-1, 1]^{32 \times 32 \times 3}$
$128 \rightarrow 4 \times 4 \times 256$, dense, linear	ResBlock down 128
ResBlock up 256	ResBlock down 128
ResBlock up 256	ResBlock 128
ResBlock up 256	ResBlock 128
BN, ReLU, 3×3 conv, 3 Tanh	ReLU
	Global sum pooling
	$h = 128 \rightarrow m$, dense, linear, Normalize

Table 9: ResNet architecture for the CelebA and LSUN datasets.

(a) Generator G_{θ}	(b) Navigator \mathcal{T}_{ϕ} / Critic \mathcal{T}_{η}
$\epsilon \in \mathbb{R}^{128} \sim \mathcal{N}(0, 1)$	$\mathbf{x} \in [-1, 1]^{64 \times 64 \times 3}$
$128 \rightarrow 4 \times 4 \times 1024$, dense, linear	ResBlock down 128
ResBlock up 512	ResBlock down 256
ResBlock up 256	ResBlock down 512
ResBlock up 128	ResBlock down 1024
ResBlock up 64	ReLU
BN, ReLU, 3×3 conv, 3 Tanh	Global sum pooling
	$h = 1024 \rightarrow m$, dense, linear, Normalize

Table 10: ResNet architecture for the LSUN-128 dataset.

(a) Generator G_{θ}	(b) Navigator \mathcal{T}_{ϕ} / Critic \mathcal{T}_{η}
$\epsilon \in \mathbb{R}^{128} \sim \mathcal{N}(0, 1)$	$\mathbf{x} \in [-1, 1]^{64 \times 64 \times 3}$
$128 \rightarrow 4 \times 4 \times 1024$, dense, linear	ResBlock down 128
ResBlock up 1024	ResBlock down 256
ResBlock up 512	ResBlock down 512
ResBlock up 256	ResBlock down 1024
ResBlock up 128	ResBlock 1024
ResBlock up 64	ReLU
BN, ReLU, 3×3 conv, 3 Tanh	Global sum pooling
	$h = 1024 \rightarrow m$, dense, linear, Normalize

Table 11: ResNet architecture for the CelebA-HQ dataset.

(a) Generator G_{θ}	(b) Navigator \mathcal{T}_{ϕ} / Critic \mathcal{T}_{η}
$\epsilon \in \mathbb{R}^{128} \sim \mathcal{N}(0, 1)$	$\mathbf{x} \in [-1, 1]^{64 \times 64 \times 3}$
$128 \rightarrow 4 \times 4 \times 1024$, dense, linear	ResBlock down 128
ResBlock up 1024	ResBlock down 256
ResBlock up 512	ResBlock down 512
ResBlock up 512	ResBlock down 512
ResBlock up 256	ResBlock down 1024
ResBlock up 128	ResBlock 1024
ResBlock up 64	ReLU
BN, ReLU, 3×3 conv, 3 Tanh	Global sum pooling
	$h = 1024 \rightarrow m$, dense, linear, Normalize